A virtual vertical reference concept for aided inertial navigation at the sea surface[☆]

Torleiv H. Bryne[a,*], Robert H. Rogne[a], Thor I. Fossen[a], Tor A. Johansen[a]

[a]*Department of Engineering Cybernetics, Norwegian University of Science and Technology, N-7491 Trondheim, Norway*

Abstract

When trying to capture the heaving motion of a marine vessel in waves, conventional position references such as global navigation satellite systems fall short in many cases. Because of design and satellite geometry, the vertical position measurement is typically inferior in both accuracy and precision compared to its horizontal counterparts. For aiding an inertial navigation system (INS), using conventional vertical position references may therefore be suboptimal. This article presents an alternative algorithm utilizing a virtual vertical reference (VVR) concept, based on the mean sea level, to aid the INS. The novelty of the algorithm arises where the VVR concept is augmented with an error model, used to improve the heave estimation performance. The motion of the vessel is estimated using an INS, employing a feedback-interconnected observer framework, based on nonlinear theory. The INS, using low-cost micro-electro-mechanical-system-based inertial measurement units, provides position, velocity and attitude in a dead-reckoning fashion, and is aided by a horizontal position reference, the VVR, and a compass to prevent the estimates from drifting. The estimation performance obtained with the observer structure is evaluated using Monte Carlo simulations and compared to preceding results. The algorithm is also validated experimentally and compared to an industry standard vertical reference unit using data collected on board an offshore vessel.

Keywords: Marine systems, Inertial navigation, Motion estimation, Nonlinear observers

1. Introduction

During marine operations, oceanographic research and transportation at sea, access to precise and accurate vessel motion data is vital in carrying out activities in a safe and efficient manner. Lever-arm compensation of position measurements, attitude corrections of onboard antennas, heave corrections of oceanographic data and heave compensation of cranes are examples of scenarios where knowledge of the vessel motions is necessary. Motion data is also used by onboard decision support systems, providing e.g. sea state and operability predictions and vessel capability analysis. An inertial navigation system (INS) is able to provide the motion data through estimation of position, velocity and attitude (PVA). INSs are based on inertial measurements, such as rate gyro and specific force measurements provided by an inertial measurement unit (IMU). These measurements are integrated once and twice, respectively, using a kinematic model in a dead-reckoning (DR) fashion. Due to the integration of sensor errors, such as biases and noise, aiding is applied to prevent the states of the INS from drifting.

Cost-effective integrated strapdown INSs based on micro-electro-mechanical system (MEMS) inertial sensing technology are receiving more and more attention. Due to low weight, low cost, high output frequency and where aiding is easily applied through software corrections, cost-effective and high-accuracy motion data can be obtained without installing a large INS platform. When operating marine surface craft, position reference (PosRef) systems such as global navigation satellite systems (GNSS), hydroacoustic positioning reference (HPR), together with other local PosRef systems, may be applied to counter the mentioned INS drift. However, for marine surface craft, sole usage of conventional GNSS aiding (or HPR) is not optimal due to the low precision of the vertical position measurements compared their the horizontal counterparts. This is due to, among other, the geometry of the baselines of such systems. Therefore custom heave estimators are designed to circumvent this issue, usually without any GNSS measurements. One example is Godhavn (1998), where an IMU was utilized together with a bandpass filter motivated by that the average heave position of a marine surface craft is zero. The technique of Godhavn (1998) was modified by Richter et al. (2014) to compensate for amplitude and phase errors by using additional adaptive filters. Another heave estimation strategy, based on the assumption that the heave motion could be described by a sum of cosines, while applying an accelerometer, was presented in Küchler et al. (2011) and also applied in Auestad et al. (2013).

1.1. The virtual vertical reference concept

The virtual vertical reference (VVR) concept was introduced in Bryne et al. (2014, 2015) as vertical aid to a full six-degree-

*Corresponding author

Email addresses: `Torleiv.H.Bryne@ntnu.no` (Torleiv H. Bryne), `Robert.Rogne@ntnu.no` (Robert H. Rogne), `Thor.Fossen@ntnu.no` (Thor I. Fossen), `Tor.Arne.Johansen@ntnu.no` (Tor A. Johansen)

of-freedom (6-DOF) strapdown INS without any vertical GNSS measurements, based on the same vessel constraint as in Godhavn (1998); that the vertical heave displacement of a marine surface craft is zero on average relative the mean sea surface. The VVR was introduced by exploiting the previous GNSS/INS integration framework of Grip et al. (2013), applying a feedback-interconnected structure of a linear and a nonlinear observer (NLO), and customizing it for marine surface craft utilization. The NLO provides the attitude, while the linear translational motion observer (TMO) estimates position, linear velocity and specific force. The mentioned framework was the continuation of the initial work of Grip et al. (2012b) merged with the work done by Mahony et al. (2008); Grip et al. (2012a).

The VVR concept is defined as

$$y_{\text{VVR}} := \lim_{T \to \infty} \frac{1}{T} \int_0^T d_{\text{heave}}(t)\, dt = 0. \tag{1}$$

A similar definition is used in Godhavn (1998), where d_{heave} is heave displacement of the vessel about the mean sea surface.

Even though the VVR measurement, $y_{\text{VVR}} = 0$, is perfect w.r.t. to noise, it is only accurate in average, hence suboptimal w.r.t. to heave peak-to-peak precision even when applying small gains associated with the VVR-based innovations in the aided INS. Thus, the heave estimation performance obtained in Bryne et al. (2014, 2015) may be improved, while maintaining the 6-DOF vessel motion estimates from the INS.

An alternative to the VVR concept, with potentially higher accuracy, is real-time kinematic (RTK) GNSS as presented in Godhavn (2000). However, the coverage of RTK is limited at sea and the real-time availability requirement is not necessarily guaranteed.

1.2. Main contribution

This article is an extension of the results from Bryne et al. (2014, 2015). The novelty of this work is the introduction of a VVR measurement error model. This model is applied in order to take into account the inherent short-term inaccuracy of the zero VVR measurement. The main contributions of the article are summarized as follows:

- A full 6-DOF strapdown INS with embedded high-accuracy and high-precision heave estimation. The heave estimation performance is increased compared to Bryne et al. (2014, 2015) by introducing the VVR error model.

- The origin of the nonlinear feedback-interconnected observer's error dynamics is proven semiglobal exponentially stable (USGES).

- The NLO structure, including the VVR error model, is evaluated through Monte Carlo simulations and validated using full-scale data collected on an offshore vessel operating in the Norwegian Sea.

In addition, the typical performance of three different methods used to obtain the parameters of the VVR error model is illustrated. Moreover, it is shown that the industry standard heave
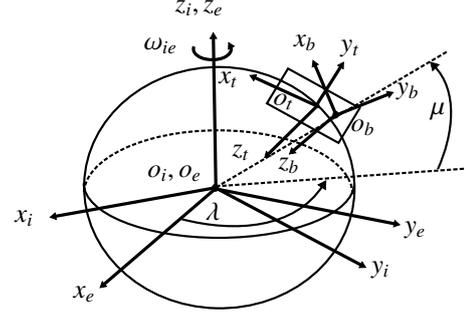

Figure 1: Definitions of the BODY, tangent, ECEF and ECI coordinate frames.

performance metric of five cm or five per cent root-mean-square (RMS) error, whichever is higher, can be obtained with the proposed observer. Bryne et al. (2015) is in the reminder of the text referred to as the *preceding observer* when comparing the performance to that obtained with the observer presented in this article.

2. Preliminaries

2.1. Notation

The Euclidean vector norm is denoted $\|\cdot\|_2$. The $n \times n$ identity matrix is denoted $\boldsymbol{I}_n$, while a block diagonal matrix is given by $\boldsymbol{M} = \text{blockdiag}(\boldsymbol{M}_1, \boldsymbol{M}_2, \ldots, \boldsymbol{M}_n)$ for square matrices $\boldsymbol{M}_1$ to $\boldsymbol{M}_n$. Moreover, the transpose of a vector or a matrix is denoted $(\cdot)^{\mathsf{T}}$. Coordinate frames are denoted with $\{\cdot\}$. $\boldsymbol{S}(\cdot) \in SS(3)$ represents the skew symmetric matrix such that $\boldsymbol{S}(z_1)z_2 = z_1 \times z_2$ for two vectors $z_1, z_2 \in \mathbb{R}^3$. $\boldsymbol{z} = (z_1; z_2; \ldots; z_n)$ denotes a vector of stacked column vectors $z_1, z_2, \ldots z_n$. In addition, $z_{bc}^a \in \mathbb{R}^3$ denotes a vector $\boldsymbol{z}$, to frame $\{c\}$, relative $\{b\}$, decomposed in $\{a\}$. Moreover, $\otimes$ denotes the Hamiltonian quaternion product. Saturation is represented by $\text{sat}_\star$, where the subscript indicates the saturation limit. The right Moore-Penrose pseudoinverse is denoted $(\cdot)^\dagger$.

The rotation matrix describing the rotation between two given frames $\{a\}$ and $\{b\}$ is denoted $\boldsymbol{R}_a^b \in SO(3)$. Similar to the rotation matrix, the rotation between $\{a\}$ and $\{b\}$ may be represented using the unit quaternion $\boldsymbol{q}_a^b = (s, \boldsymbol{r}^{\mathsf{T}})^{\mathsf{T}}$ where $s \in \mathbb{R}^1$ is the real part of the quaternion and $\boldsymbol{r} \in \mathbb{R}^3$ is the vector part. Moreover, its conjugate is denoted $\boldsymbol{q}_a^{b*} = (s, -\boldsymbol{r}^{\mathsf{T}})^{\mathsf{T}}$.

2.2. Coordinate reference frames

This article employs four coordinate frames; The Earth-Centered-Inertial (ECI) frame, the Earth-Centered-Earth-Fixed (ECEF) frame, a tangent frame equivalent of an Earth-fixed North-East-Down (NED) frame, and the BODY reference frame, denoted $\{i\}$, $\{e\}$, $\{t\}$ and $\{b\}$, respectively (see Fig. 1). The Earth's rotation rate ω_{ie} is decomposed in the tangent frame as

$$\boldsymbol{\omega}_{ie}^t = \begin{pmatrix} \cos(\mu) \\ 0 \\ -\sin(\mu) \end{pmatrix} \omega_{ie}, \tag{2}$$

where μ is the latitude on the Earth, while $\omega_{\star\star}^\star$ represents angular velocity. The longitude is denoted λ. The tangent frame

is an Earth-fixed frame and has it's origin on the surface of WGS-84 at some latitude and longitude, where the x-axis points towards north, the y-axis points towards east, and the z-axis points downwards. The BODY frame is fixed to the vessel. The origin of {b} is located at the nominal center of gravity of the vessel. The x-axis is directed from aft to fore, the y-axis is directed to starboard and the z-axis points downwards.

Roll, pitch and yaw is denoted ϕ, θ and ψ, respectively together with their angular rates p, q and r in compliance with the SNAME (1950) notations.

2.3. Kinematic strapdown equations

The attitude representation most comprehensible for the user is the attitude between the BODY and the NED (or a tangent frame). This is also the most intuitive representation for control and lever-arm compensation purposes. Using a rotation matrix representation, the attitude kinematics in this article is given as

$$\dot{\boldsymbol{R}}_b^t = \boldsymbol{R}_b^t \boldsymbol{S}(\boldsymbol{\omega}_{ib}^b) - \boldsymbol{S}(\boldsymbol{\omega}_{it}^t)\boldsymbol{R}_b^t, \tag{3}$$

or equivalently,

$$\dot{\boldsymbol{q}}_b^t = \frac{1}{2}\boldsymbol{q}_b^t \otimes \begin{pmatrix} 0 \\ \boldsymbol{\omega}_{ib}^b \end{pmatrix} - \frac{1}{2}\begin{pmatrix} 0 \\ \boldsymbol{\omega}_{it}^t \end{pmatrix} \otimes \boldsymbol{q}_b^t, \tag{4}$$

using the unit quaternion attitude representation. $\boldsymbol{\omega}_{ib}^b$ is the angular rate of the navigating object relative the inertial frame, while $\boldsymbol{\omega}_{it}^t$ is the angular velocity of navigation frame relative the inertial frame where,

$$\boldsymbol{\omega}_{it}^t = \boldsymbol{\omega}_{ie}^t + \boldsymbol{\omega}_{et}^t. \tag{5}$$

However, $\boldsymbol{\omega}_{et}^t = \boldsymbol{0}_{3\times1}$ since the tangent frame is Earth fixed. Furthermore, from Fossen (2011), Eq. (2.56) and reference therein, the rotation matrix $\boldsymbol{R}(\boldsymbol{q}_b^t) := \boldsymbol{R}_b^t$ is obtained from $\boldsymbol{q}_b^t$ using

$$\boldsymbol{R}(\boldsymbol{q}_b^t) = \boldsymbol{I}_3 + 2s\boldsymbol{S}(\boldsymbol{r}) + 2\boldsymbol{S}(\boldsymbol{r}). \tag{6}$$

When using the tangent frame as the navigation frame, the rotational and translational motion is related with

$$\dot{\boldsymbol{p}}_{tb}^t = \boldsymbol{v}_{tb}^t, \tag{7}$$

$$\dot{\boldsymbol{v}}_{tb}^t = -2\boldsymbol{S}(\boldsymbol{\omega}_{ie}^t)\boldsymbol{v}_{tb}^t + \boldsymbol{R}_b^t\boldsymbol{f}_{ib}^b + \boldsymbol{g}_b^t, \tag{8}$$

(Farrell, 2008), where $\boldsymbol{p}_{tb}^t \in \mathbb{R}^3$ is the position, relative the defined origin of the tangent frame. Furthermore, $\boldsymbol{v}_{tb}^t \in \mathbb{R}^3$ is the linear velocity. It follows that $\boldsymbol{g}_b^t(\mu, \lambda) \in \mathbb{R}^3$ is the local gravity vector which may be obtained using a gravity model based on the vessel's latitude and longitude. $\boldsymbol{f}_{ib}^b = (\boldsymbol{R}_b^t)^\mathsf{T}(\boldsymbol{a}_{ib}^t - \boldsymbol{g}_b^t) \in \mathbb{R}^3$ is the specific force decomposed in {b}, where $\boldsymbol{a}_{ib}^t$ is the acceleration vector decomposed in the tangent frame.

2.4. Sensor models

2.4.1. Inertial measurements

The tri-axial IMU sensor model is chosen as

$$\boldsymbol{\omega}_{\mathrm{IMU}}^b = \boldsymbol{\omega}_{ib}^b + \boldsymbol{b}_{\mathrm{gyro}}^b + \boldsymbol{\varepsilon}_{\mathrm{gyro}}, \tag{9}$$

$$\dot{\boldsymbol{b}}_{\mathrm{gyro}}^b = \boldsymbol{0}, \tag{10}$$

$$\boldsymbol{f}_{\mathrm{IMU}}^b = \boldsymbol{f}_{ib}^b + \boldsymbol{\varepsilon}_{\mathrm{acc}}, \tag{11}$$

where $\boldsymbol{\varepsilon}_\star$ denotes sensor noise and $\boldsymbol{b}_{\mathrm{gyro}}^b$ denotes the rate gyro bias. The accelerometer bias is assumed to be compensated for in calibration. According to the results of Bryne et al. (2016) this is a valid assumption in the context of attitude estimation.

For many rate gyros (such as MEMS based) a more accurate term would be angular rate sensor (ARS) since often none of the sensor's parts are rotating. Nevertheless, the term *gyro* or *rate gyro* was chosen for this work, since it is in compliance with the established literature, (Titterton and Weston, 2004; Farrell, 2008; Groves, 2013).

2.4.2. Position reference system

The PosRef measurement is modeled as

$$\boldsymbol{p}_{tb,\mathrm{PosRef}}^t = \boldsymbol{p}_{tb,xy}^t + \boldsymbol{\varepsilon}_{\mathrm{PosRef}}, \tag{12}$$

where $\boldsymbol{p}_{tb,xy}^t$ represents the true horizontal position of the vessel, while $\boldsymbol{\varepsilon}_{\mathrm{PosRef}}$ represents noise and errors.

2.5. Compass

The compass measurement is modeled as

$$\psi_c = \psi + \varepsilon_\psi, \tag{13}$$

where ψ represents the heading relative north, while ε_ψ constitutes noise and errors.

2.5.1. Virtual vertical reference

For marine surface vessels, the kinematics of (7)–(8) can further be extended with the auxiliary variable $p_{tb,I}^t$. The augmentation, first applied in Bryne et al. (2014), is motivated above in Sec. 1.1. $p_{tb,I}^t$ is introduced by first writing (1) as

$$\lim_{T\to\infty} \frac{1}{T} \int_0^T p_{tb,z}^t(t)\,\mathrm{d}t = 0, \tag{14}$$

applying the notation of Sec. 2.1. Based on (14) the strapdown equations (7)–(8) are augmented with $p_{tb,I}^t$ as an auxiliary state by defining

$$\dot{p}_{tb,I}^t := p_{tb,z}^t, \tag{15}$$

thus, integrating the vertical (down) position, $p_{tb,z}^t$, associated with the heave motion. Then a natural choice would be to exploit (14) and define a virtual vertical reference (VVR) measurement (Bryne et al., 2014, 2015) by choosing

$$y_{VVR}^t = p_{tb,I}^t = 0, \quad \forall t \geq 0. \tag{16}$$

However, as indicated in (14), this would only be valid on average. Hence, (16) is a very precise, but not necessarily a very accurate measurement. Especially so in high sea states where the amplitude of the wave-induced craft motion is high and the frequency of the motion is low (Fossen, 2011, Ch. 8) resulting in longer time intervals where $y_{\mathrm{vvr}}^t \neq p_{tb,I}^t$. Therefore, the VVR measurement would be less desirable to apply in such conditions. This issue is not dealt with in the previous works of Bryne et al. (2014, 2015). The proposed solution for this problem is presented next.

Fossen and Perez (2009), states that all sensors measuring some vessel motion contain both the low-frequency (LF) and wave-frequency (WF) motion of the vessel. However, y^t_{VVR} of (16) only contains the former. This makes it, in some sense, biased. In order to improve the general accuracy of $y_{VVR} = 0$, w.r.t. $p^t_{tb,I}$, additional sensor error parameters are introduced by stating

$$y^t_{VVR} = p^t_{tb,I} + b^t_{tb,I} = 0, \tag{17}$$

where the dynamics of $b^t_{tb,I}$ is inspired by the works on wave-filtering of estimated vessel motion such as Sælid et al. (1983), Fossen and Strand (1999) and Fossen and Perez (2009). The VVR error model takes the form of

$$\dot{\zeta}^t_{tb} = b^t_{tb,I}, \tag{18}$$

$$\dot{b}^t_{tb,I} = -\omega^2_e(t)\zeta^t_{tb} - 2\lambda_w(t)\omega_e(t)b^t_{tb,I} + \sigma_{b,VVR}\varepsilon_u, \tag{19}$$

for some auxiliary state ζ^t_{tb}, where $0 < \lambda_w(t) < 1$ is the relative damping ratio of the wave-induced motion and

$$\omega_e(t, U, \omega_0, \beta) = \left| \omega_0 - U \frac{\omega^2_0}{g} \cos(\beta) \right|, \tag{20}$$

being the encounter frequency of the waves experienced by the ship (Fossen, 2011, Ch. 8.2.3). Here U is the horizontal speed of the vessel, ω_0 is the peak frequency of the wave spectrum, $g = \|g^t_b\|_2$ and β is the angle between the heading of the vessel and the direction of the waves. $\sigma_{b,VVR}$ is the standard deviation of the process noise and is considered a tuning parameter related to the heave amplitude. In practice, its magnitude is also a measure of how much the model structure and its parameters are trusted. Finally, ε_u represents unity white noise.

3. Nonlinear observer for integrated inertial navigation

The motion of the marine surface craft is estimated using a feedback-interconnected nonlinear observer integration strategy as depicted in Fig. 2. The PVA estimation is carried out in two steps. First the attitude is estimated by using rate gyro, specific force and compass measurements. The attitude observer is further aided by the second step, consisting of a TMO providing specific force estimates in the navigation frame, together with 3-DOF position and velocity estimates based on the estimated attitude, in addition to, specific force, PosRef and VVR measurements.

3.1. Attitude observer

The NLO for estimating the attitude between the $\{b\}$ and the $\{t\}$ frame is given similar to Grip et al. (2013),

$$\Sigma_1 : \begin{cases} \dot{\hat{q}}^t_b = \frac{1}{2}\hat{q}^t_b \otimes \begin{pmatrix} 0 \\ \hat{\omega}^b_{ib} \end{pmatrix} - \frac{1}{2}\begin{pmatrix} 0 \\ \omega^t_{it} \end{pmatrix} \otimes \hat{q}^t_b, & (21a) \\ \hat{\omega}^b_{ib} = \omega^b_{IMU} - \hat{b}^b_{gyro} + \hat{\sigma}^b_{ib}, & (21b) \\ \dot{\hat{b}}^b_{gyro} = \text{Proj}\left(\hat{b}^b_{gyro}, -k_I\hat{\sigma}^b_{ib}\right), & (21c) \end{cases}$$

where $\text{Proj}(\star, \star)$ denotes the angular rate bias projection algorithm ensuring that $\|\hat{b}^b_{gyro}\|_2 \leq M_{\hat{b}_{gyro}}$ for $M_{\hat{b}_{gyro}} > M_{b_{gyro}}$ (Grip et al., 2012a), and k_I is the gain associated with the rate gyro bias estimation. The NLO is structurally the same as in Grip et al. (2013), where the attitude between the $\{b\}$ and the $\{e\}$ frame was estimated. Moreover, the observer's nonlinear injection term, $\hat{\sigma}^b_{ib}$, is given as

$$\hat{\sigma}^b_{ib} = k_1 \underline{v}^b_1 \times R^\mathsf{T}(\hat{q}^t_b)\underline{v}^t_1 + k_2 \underline{v}^b_2 \times R^\mathsf{T}(\hat{q}^t_b)\underline{v}^t_2, \tag{22}$$

where the measurement vectors $\underline{v}^b_{1,2}$ and reference vectors $\underline{v}^t_{1,2}$ are calculated using

$$\underline{v}^b_1 = \underline{f}^b, \qquad \underline{v}^t_1 = \underline{f}^t, \tag{23}$$

$$\underline{v}^b_2 = \underline{f}^b \times \underline{c}^b, \qquad \underline{v}^t_2 = \underline{f}^t \times \underline{c}^t. \tag{24}$$

Furthermore, the measurement and corresponding reference vector pairs in (23)–(24) are constructed as

$$\underline{f}^b = \frac{f^b_{IMU}}{\|f^b_{IMU}\|_2}, \qquad \underline{f}^t = \frac{\text{sat}_{M_f}(\hat{f}^t_{ib})}{\|\text{sat}_{M_f}(\hat{f}^t_{ib})\|_2}, \tag{25}$$

$$\underline{c}^b = \begin{pmatrix} \cos\psi_c & -\sin(\psi_c) & 0 \end{pmatrix}^\mathsf{T}, \qquad \underline{c}^t = \begin{pmatrix} 1 & 0 & 0 \end{pmatrix}^\mathsf{T}. \tag{26}$$

$\hat{f}^t_{ib}$ is the estimated specific force, provided by the TMO, presented next in Sec. 3.2, as depicted in Fig. 2. The benefit of using normalized vectors is that the vector pairs only provide direction, hence these are dimensionless, such that the gains $k_{1,2}$ can be considered as cut-off frequencies of the complementary filter Σ_1, (Hua et al., 2014). Since the gains have unit rad/s, $\hat{\sigma}^b_{ib}$ obtains the same unit as ω^b_{IMU}.

The estimation error is defined as $\tilde{q} := q^t_b \otimes \hat{q}^{t*}_b$ and $\tilde{b}^b = b^b_{gyro} - \hat{b}^b_{gyro}$. Furthermore, $\chi := (\tilde{r}; \tilde{b}^b)$ is defined, where $\tilde{r}$ denotes the vector part of $\tilde{q}$. Semiglobal exponential stability of the origin $\chi = 0$ ($\tilde{s} = 1$ of the scalar part of $\tilde{q}$) of the attitude observer's error dynamics can be established under the following three assumptions:

Assumption 1. *The angular rate ω^b_{ib}, the specific force f^b_{ib} and its rate $\dot{f}^b_{ib}$ are uniformly bounded.*

Assumption 2. *There exist a constant $c_{obs} > 0$ such that $\|\underline{f}^b \times \underline{c}^b\|_2 \geq c_{obs}$ for all $t \geq 0$, resulting in the attitude being uniformly observable.*

Assumption 3. *The initial condition is assumed to be contained in the set $\mathcal{D}(\epsilon) = \{\tilde{q} \mid |\tilde{s}| > \epsilon\}$, i.e. $\hat{q}^t_b(0) \in \mathcal{D}$, representing attitude errors bounded away from $180°$ by a margin determined by $\epsilon \in (0, \frac{1}{2})$. Furthermore, it is assumed that $\hat{b}^b_{gyro}(0)$ is projected to the ball $\mathcal{B} \in \{b^b_{gyro} \mid \|b^b_{gyro}\|_2 \leq M_{b_{gyro}}\}$.*

From Assumptions 1–3, the result of Grip et al. (2012a) is used, where, for each $\epsilon \in (0, \frac{1}{2})$, there exsist a $k^*_p > 0$ such that if $k_1, k_2 > k^*_p$ and a $k_I > 0$, yielding

$$\|\chi(t)\|_2 \leq \kappa_a e^{-\lambda_a t}\|\chi(0)\|_2, \quad \forall t \geq 0, \tag{27}$$

for some $\kappa_a, \lambda_a > 0$ where $\chi(0) \in \{\mathcal{D}(\epsilon), \mathcal{B}\}$, resulting in the origin of χ is USGES if $\hat{f}^t_{ib} = f^t_{ib}$. Estimation of f^t_{ib} is carried out next by the TMO.
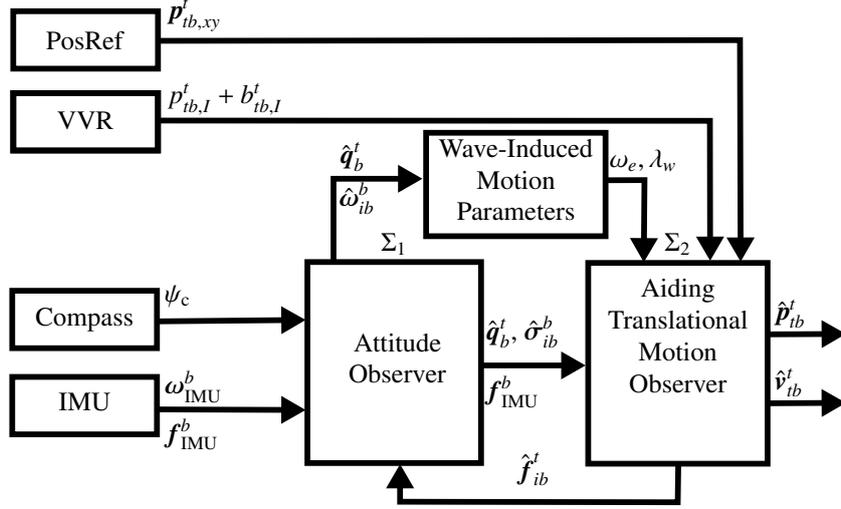
4

Figure 2: NLO structure overview

3.2. Translational motion observer (TMO)

The TMO is inspired by the previous work of Grip et al. (2012b, 2013), and is an augmentation of the preceding TMO of Bryne et al. (2015), given as follows,

$$\Sigma_2 : \begin{cases} \dot{\hat{p}}_{tb,I}^t = \hat{p}_{tb,z}^t + \vartheta K_{p_I p_I}^0 \tilde{y}_{tb,I}^t & (28a) \\ \dot{\hat{p}}_{tb}^t = \hat{v}_{tb}^t + \vartheta^2 \begin{pmatrix} \mathbf{0}_{2\times1} \\ K_{pp_I}^0 \end{pmatrix} \tilde{y}_{tb,I}^t + \vartheta \begin{pmatrix} K_{pp}^0 \\ \mathbf{0}_{1\times2} \end{pmatrix} \tilde{y}_{tb,xy}^t & (28b) \\ \dot{\hat{v}}_{tb}^t = -2S(\omega_{ie}^t)v_{tb}^t + \hat{f}_{ib}^t + g_b^t \\ \qquad + \vartheta^3 \begin{pmatrix} \mathbf{0}_{2\times1} \\ K_{vp_I}^0 \end{pmatrix} \tilde{y}_{tb,I}^t + \vartheta^2 \begin{pmatrix} K_{vp}^0 \\ \mathbf{0}_{1\times2} \end{pmatrix} \tilde{y}_{tb,xy}^t & (28c) \\ \dot{\xi}_{ib}^t = -R(\hat{q}_b^t)S(\hat{\sigma}_{ib}^b)f_{IMU}^b \\ \qquad + \vartheta^4 \begin{pmatrix} \mathbf{0}_{2\times1} \\ K_{\xi p_I}^0 \end{pmatrix} \tilde{y}_{tb,I}^t + \vartheta^3 \begin{pmatrix} K_{\xi p}^0 \\ \mathbf{0}_{1\times2} \end{pmatrix} \tilde{y}_{tb,xy}^t & (28d) \\ \hat{f}_{ib}^t = R(\hat{q}_b^t)f_{IMU}^b + \xi_{ib}^t, & (28e) \\ \dot{\hat{\zeta}}_{tb}^t = \hat{b}_{tb,I}^t + K_{\zeta p_I}^0 \tilde{y}_{tb,I}^t & (28f) \\ \dot{\hat{b}}_{tb,I}^t = -\omega_e^2(t)\hat{\zeta}_{tb}^t - 2\lambda_w(t)\omega_e(t)\hat{b}_{tb,I}^t + K_{b_I p_I}^0 \tilde{y}_{tb,I}^t & (28g) \end{cases}$$

where $\tilde{y}_{tb,I}^t = p_{VVR}^t - (\hat{p}_{tb,I}^t + \hat{b}_{tb,I}^t)$ and $\tilde{y}_{tb,xy}^t = p_{PosRef}^t - \hat{p}_{tb,xy}^t$, while $K_\star$ and $\mathbf{K}_\star$ are gains associated with the VVR and the horizontal PosRef measurements, respectively. ξ_{ib}^t is an auxiliary state used to estimate f_{ib}^t. ϑ is a high-gain like parameter used to guarantee stability. The extension of the previous work is the introduction of (28f)–(28g) to Σ_2, based on the error model presented in Sec. 2.5.1. This is done to atone for the inaccuracies of the VVR measurement w.r.t. $p_{tb,I}^t$. As a contrast to the cited works on wave filtering, where the LF motion is estimated from measurements containing LF and WF motion, Σ_2 estimates the WF heave motion based on the inherent LF zero VVR measurement. Furthermore, by noting the linear time-varying (LTV) structure of (28) and defining

$$x := \begin{pmatrix} p_{tb,I}^t; & p_{tb}^t; & v_{tb}^t; & \xi_{ib}^t; & \zeta_{tb}^t; & b_{tb,I}^t \end{pmatrix}, \quad (29)$$

the TMO can be written on LTV form as

$$\dot{\hat{x}} = A(t)\hat{x} + B(t)u + D(t,\hat{x}) + K(t)(y - C\hat{x}), \quad (30)$$

with the system matrices,

$$A(t) = \text{blockdiag}(A^*, F_{VVR}(t)), \quad (31a)$$

$$A^* = \begin{pmatrix} 0 & 0\,0\,1 & \mathbf{0}_{1\times3} & \mathbf{0}_{1\times3} \\ \mathbf{0}_{3\times1} & \mathbf{0}_{3\times3} & I_3 & \mathbf{0}_{3\times3} \\ \mathbf{0}_{3\times1} & \mathbf{0}_{3\times3} & \mathbf{0}_{3\times3} & I_3 \\ \mathbf{0}_{3\times1} & \mathbf{0}_{3\times3} & \mathbf{0}_{3\times3} & \mathbf{0}_{3\times3} \end{pmatrix}, \quad (31b)$$

$$F_{VVR}(t) = \begin{pmatrix} 0 & 1 \\ -\omega_e^2(t) & -2\lambda_w(t)\omega_e(t) \end{pmatrix}, \quad (31c)$$

input matrices,

$$B(t) = \begin{pmatrix} B^*(t) \\ \mathbf{0}_{2\times6} \end{pmatrix}, \quad B^*(t) = \begin{pmatrix} \mathbf{0}_{1\times3} & \mathbf{0}_{1\times3} \\ \mathbf{0}_{3\times3} & \mathbf{0}_{3\times3} \\ R(\hat{q}_b^t) & \mathbf{0}_{3\times3} \\ \mathbf{0}_{3\times3} & R(\hat{q}_b^t) \end{pmatrix}, \quad (32)$$

the measurement matrices,

$$C = \begin{pmatrix} C^* & H_{VVR} \\ & \mathbf{0}_{2\times2} \end{pmatrix}, C^* = \begin{pmatrix} I_3 & \mathbf{0}_{3\times7} \end{pmatrix}, H_{VVR} = \begin{pmatrix} 0 & 1 \end{pmatrix}, \quad (33)$$

the vector,

$$D(t,\hat{x}) = \begin{pmatrix} 0; & \mathbf{0}_{3\times1}; & -2S(\omega_{ie}^t)\hat{v}_{tb}^t + g_b^t; & \mathbf{0}_{3\times1}; & \mathbf{0}_{2\times1} \end{pmatrix}, \quad (34)$$

and the gain matrix,

$$K(t) = \begin{pmatrix} K_{p_I p_I} & \mathbf{0}_{1\times2} \\ \mathbf{0}_{2\times1} & K_{pp} \\ K_{pp_I} & \mathbf{0}_{1\times2} \\ \mathbf{0}_{2\times1} & K_{vp} \\ K_{vp_I} & \mathbf{0}_{1\times2} \\ \mathbf{0}_{2\times1} & K_{\xi p} \\ K_{\xi p_I} & \mathbf{0}_{1\times2} \\ K_{\zeta p_I} & \mathbf{0}_{1\times2} \\ K_{b_I p_I} & \mathbf{0}_{1\times2} \end{pmatrix} = \begin{pmatrix} \vartheta K_{p_I p_I}^0 & \mathbf{0}_{1\times2} \\ \mathbf{0}_{2\times1} & \vartheta K_{pp}^0 \\ \vartheta^2 K_{pp_I}^0 & \mathbf{0}_{1\times2} \\ \mathbf{0}_{2\times1} & \vartheta^2 K_{vp}^0 \\ \vartheta^3 K_{vp_I}^0 & \mathbf{0}_{1\times2} \\ \mathbf{0}_{2\times1} & \vartheta^3 K_{\xi p}^0 \\ \vartheta^4 K_{\xi p_I}^0 & \mathbf{0}_{1\times2} \\ K_{\zeta p_I}^0 & \mathbf{0}_{1\times2} \\ K_{b_I p_I}^0 & \mathbf{0}_{1\times2} \end{pmatrix}. \quad (35)$$

5

Finally, the input is given as

$$u = \left(f_{\text{IMU}}^b; -S(\hat{\sigma}_{ib}^b) f_{\text{IMU}}^b \right). \tag{36}$$

Moreover, the error states of the TMO can be defined as $\tilde{p}_{tb,I}^t := p_{tb,I}^t - \hat{p}_{tb,I}^t$, $\tilde{p}_{tb}^t := p_{tb}^t - \hat{p}_{tb}^t$, $\tilde{v}_{tb}^t := v_{tb}^t - \hat{v}_{tb}^t$, and $\tilde{f}_{tb}^t := f_{ib}^t - \hat{f}_{ib}^t$, where the latter is obtained through a combination of (28d)–(28e). By including the auxiliary states, associated with the VVR error, $\tilde{\zeta}_{tb}^t := \zeta_{tb}^t - \hat{\zeta}_{tb}^t$ and $\tilde{b}_{tb,I}^t := b_{tb,I}^t - \hat{b}_{tb,I}^t$, the resulting the error state space is obtained,

$$\tilde{x} := \left(\tilde{p}_{tb,I}^t; \quad \tilde{p}_{tb}^t; \quad \tilde{v}_{tb}^t; \quad \tilde{f}_{ib}^t; \quad \tilde{\zeta}_{tb}^t; \quad \tilde{b}_{tb,I}^t \right). \tag{37}$$

The corresponding error dynamics of the origin of Σ_2 is then obtained as

$$\dot{\tilde{x}} = (A(t) - K(t)C)\tilde{x} + \rho_1(t, \tilde{x}) + \rho_2(t, \chi), \tag{38}$$

with

$$\rho_1(t, \tilde{x}) = \left(0; \quad \mathbf{0}_{3\times1}; \quad -2S(\omega_{ie}^t)\tilde{v}_{tb}^t; \quad \mathbf{0}_{3\times1}; \quad \mathbf{0}_{2\times1} \right), \tag{39}$$

$$\rho_2(t, \chi) = \left(0; \quad \mathbf{0}_{3\times1}; \quad \mathbf{0}_{3\times1}; \quad \tilde{d}(t, \chi); \quad \mathbf{0}_{2\times1} \right), \tag{40}$$

and where,

$$\tilde{d}(t, \chi) = (I_3 - R(\tilde{q})^\mathsf{T}) R_b^t \left(S(\omega_{ib}^b) f_{ib}^b + \dot{f}_{ib}^b \right) \\ - S(\omega_{it}^t)(I_3 - R^\mathsf{T}(\tilde{q})) R_b^t f_{ib}^b - R^\mathsf{T}(\tilde{q}) R_b^t S(\tilde{b}_{\text{gyro}}^b) f_{ib}^b, \tag{41}$$

similar to Grip et al. (2013) and Johansen et al. (2017). In order to apply $\vartheta \geq 1$ to estimate f_{ib}^t in the presence of disturbance of (41), the system (30) has to be left invertible. This was verified using the results of Grip and Saberi (2010) and the accompanying Maple toolbox.

3.3. Stability analysis

As in Grip et al. (2013), Bryne et al. (2014, 2015), Johansen et al. (2017), a parameter $\vartheta \geq 1$ is utilized to assign a certain time-scale structure to the error dynamics (38). For this purpose, the non-singular transform

$$L_\vartheta = \text{blockdiag}\left(1, \frac{1}{\vartheta}I_3, \frac{1}{\vartheta^2}I_3, \frac{1}{\vartheta^3}I_3, I_2\right), \tag{42}$$

of the error state $\tilde{x}$ is introduced such that the transformed state space is obtained using $\eta := L_\vartheta \tilde{x}$ yielding

$$\eta = \begin{pmatrix} \eta_1 \\ \eta_2 \\ \eta_3 \\ \eta_4 \\ \eta_5 \end{pmatrix} = \begin{pmatrix} \tilde{p}_{tb,I}^t \\ \frac{1}{\vartheta}\tilde{p}_{tb}^t \\ \frac{1}{\vartheta^2}\tilde{v}_{tb}^t \\ \frac{1}{\vartheta^3}\tilde{f}_{tb}^t \\ (\tilde{\zeta}_{tb}^t, \tilde{b}_{tb,I}^t) \end{pmatrix}. \tag{43}$$

Moreover, the compounded gain (35) can further be defined

$$K(t) := \vartheta L_\vartheta^{-1} K_0(t) E_\vartheta, \tag{44}$$

with $\boldsymbol{\vartheta} = \text{blockdiag}(\vartheta \cdot I_{10}, I_2)$, and where the nominal gain $K_0(t)$ and the matrix E_ϑ is obtained with

$$K_0(t) = P(t)C^\mathsf{T} R^{-1}(t), \tag{45}$$

and

$$E_\vartheta = CL_\vartheta C^\dagger, \tag{46}$$

respectively. Moreover, $P(t) = P^\mathsf{T}(t) > 0$ is the solution of the time-scaled Riccati equation,

$$\boldsymbol{\vartheta}^{-1}\dot{P}(t) = A(t)P(t) + P(t)A^\mathsf{T}(t) - P(t)C^\mathsf{T} R^{-1}(t)CP(t) \\ + G(t)Q(t)G^\mathsf{T}(t). \tag{47}$$

In addition,

$$G(t) = \begin{pmatrix} B(t) & \mathbf{0}_{10\times2} \\ & G_{\text{VVR}}(t) \end{pmatrix}, \tag{48}$$

with $G_{\text{VVR}}(t) = (0, \sigma_{b,\text{VVR}}(t))^\mathsf{T}$, and the positive definite tuning matrices $Q(t) = Q^\mathsf{T}(t) > 0$, $R(t) = R^\mathsf{T}(t) > 0$, $P(0) = P^\mathsf{T}(0) > 0$. Finally, (46) follows from Lemma 1.

Lemma 1. $E_\vartheta = CL_\vartheta C^\dagger$ *satisfies* $E_\vartheta C = CL_\vartheta$.

Proof: See Appendix A.

Now, the error dynamics of (38) can be transformed onto η yielding

$$\boldsymbol{\vartheta}^{-1}\dot{\eta} = (A(t) - K_0(t)C)\eta + \frac{1}{\vartheta}\rho_1(t, \eta) + \frac{1}{\vartheta^4}\rho_2(t, \chi), \tag{49}$$

where $\rho_1(t, \eta) = \left(0, \mathbf{0}_{3\times1}; -2S(\omega_{ie}^t)\eta_3; \mathbf{0}_{3\times1}; \mathbf{0}_{2\times1} \right)$. With the transform, the relations $L_\vartheta A(t)\tilde{x} = \boldsymbol{\vartheta}A(t)\eta$ and $L_\vartheta K(t)C\tilde{x} = \boldsymbol{\vartheta}L_\vartheta L_\vartheta^{-1} K_0(t)E_\vartheta C\tilde{x} = \boldsymbol{\vartheta}K_0(t)CL_\vartheta\tilde{x} = \boldsymbol{\vartheta}K_0(t)C\eta$ are obtained.

First, the nominal transformed dynamics are considered,

$$\boldsymbol{\vartheta}^{-1}\dot{\eta} = (A(t) - K_0(t)C)\eta, \tag{50}$$

and the accompanying observability and controllability properties that must be satisfied in order to obtain the desired stability properties.

Lemma 2. *Considering the measurement covariance matrix* $R(t)$ *and the process noise covariance matrix* $Q(t)$, *the system* $\left(A(t), R^{-1/2}(t)C \right)$ *is uniformly completely observable (UCO) and the system* $\left(A(t), Q^{1/2}(t)G(t) \right)$ *is uniformly completely controllable (UCC) for all* $0 < \lambda_w < 1$ *and positive, bounded* $\omega_e(t)$.

Proof: See Appendix B.

Since UCO and UCC is established, the stability properties of the origin of (50) can now be obtained.

Lemma 3. *Let the nominal gain* K_0 *be calculated according to (45) where* $P(t) = P^\mathsf{T}(t) > 0$ *is the solution of the time-scaled Riccati equation (47) with the positive definite matrices* $Q(t) = Q^\mathsf{T}(t) > 0$, $R(t) = R^\mathsf{T}(t) > 0$, $P(0) = P^\mathsf{T}(0) > 0$. *Then,* $P(t)$ *is uniformly bounded and the origin of (50) is globally exponentially stable (GES) for any* $\vartheta \geq 1$.

Proof: See Appendix C.

Under the conditions in Assumptions 1–2 and 4–5, the main result of this article can be obtained with Proposition 1.

Assumption 4. *Initial conditions are in the following sets:*

- $\mathcal{X} \subset \mathbb{R}^{12}$ *is a ball containing the origin* $\tilde{\boldsymbol{x}} = \boldsymbol{0}$.
- $\mathcal{P} \subset \mathbb{R}^{(12) \times (12)}$ *is an arbitrary compact set of symmetric positive definite matrices* $\boldsymbol{P}(0)$.
- $\mathcal{D}(\bar{\epsilon}) = \{\tilde{\boldsymbol{q}} \mid |\tilde{s}| > \bar{\epsilon}\}$ *presents a set of attitude errors bounded away from* $180°$ *by a small margin determined by an arbitrary constant* $\bar{\epsilon} \in \left(0, \frac{1}{2}\right)$.
- $\mathcal{B} \in \{\boldsymbol{b}_{\text{gyro}}^b \mid \|\boldsymbol{b}_{\text{gyro}}^b\|_2 \le M_{b_{\text{gyro}}}\}$.

Assumption 5. *Observer gains are chosen according to*

- $k_1, k_2 > 0$ *are sufficiently large, cf. Grip et al. (2013).*
- $k_I > 0$ *is arbitrary.*
- $\boldsymbol{K}(t)$ *is chosen according to* (44)–(45) *and is tuned using* (47) *with the matrices* $\boldsymbol{Q}(t) = \boldsymbol{Q}^\intercal(t)$, $\boldsymbol{R}(t) = \boldsymbol{R}^\intercal(t)$, $\boldsymbol{P}(0) = \boldsymbol{P}^\intercal(0) > 0$.

Propostion 1. *There exists a* $\vartheta^\star \ge 1$ *such that for all* $\vartheta \ge \vartheta^\star$, *then* $\boldsymbol{P}(t)$ *is uniformly bounded and*

$$\sqrt{\|\tilde{\boldsymbol{x}}(t)\|_2^2 + \|\boldsymbol{\chi}(t)\|_2^2} \le \kappa e^{-\lambda t} \sqrt{\|\tilde{\boldsymbol{x}}(0)\|_2^2 + \|\boldsymbol{\chi}(0)\|_2^2}, \qquad (51)$$

for some $\kappa > 0$ *and* $\lambda > 0$ *rendering the origin* $(\tilde{\boldsymbol{x}}; \boldsymbol{\chi}) = \boldsymbol{0}$ *USGES.*

Proof: See Appendix D.

4. Obtaining ω_e and λ_w

The parameters, $\omega_e(t)$ and $\lambda_w(t)$ in the VVR error model are generally unknown and have to be estimated online. Although $\lambda_w(t)$ is often chosen as 0.1 for wave-filtering in dynamic positioning (DP) operations, (Fossen, 2011, Ch. 8.2.6, 11.3.6), (Perez, 2005, Ch 12.5), during e.g. vessel transit, with changing sea states, and other situations, estimating $\lambda_w(t)$ might increase performance compared to compensating for the uncertainty in $\lambda_w(t)$ with gain-scheduling dependent on operation and/or sea state. $\omega_e(t)$ can be obtained with a variety of online methods. In this article, three methods for finding $\omega_e(t)$ are compared, where one of them also estimates $\lambda_w(t)$.

4.1. Wave frequency estimator

The encounter frequency $\omega_e(t)$ may be obtained using the GES wave frequency estimator of Belleter et al. (2015) with,

$$\dot{\zeta}_1 = \zeta_2 \qquad (52)$$
$$\dot{\zeta}_2 = -2\omega_f \zeta_2 - \omega_f^2 \zeta_1 + \omega_f^2 y_w \qquad (53)$$
$$\dot{\hat{\varphi}} = k(t)\zeta_1(\dot{\zeta}_2 - \hat{\varphi}\zeta_1) \qquad (54)$$

where y_w is the input signal, ω_f is the embedded low-pass filter's cut-off frequency, $k(t)$ is a positive, smooth time-varying gain and the parameter φ relates to $\hat{\omega}_e(t)$ with $\hat{\omega}_e(t) = \sqrt{|\varphi|}$ such that $\hat{\omega}_e(t)$ converges to $\omega_e(t)$ exponentially fast. Since $\hat{\omega}_e(t)$ is supposed to be used to improve the heave estimate, the pitch estimate was employed as the driving signal, i.e. $y_w = \hat{\theta}$, due to the strong pitch-heave coupling. Moreover, $\hat{\theta}$ is obtained from $\hat{\boldsymbol{q}}_b^t$.

4.2. Kalman filter (KF) based estimation of $\omega_e(t)$ and $\lambda_w(t)$

The encounter frequency $\omega_e(t)$ and the relative damping factor of the wave spectra, $\lambda_w(t)$, may be obtained using the algorithm of Perez (2005, Ch. 12.5), here however, based on the estimated pitch $\hat{\theta}$ and estimated pitch rate $\hat{q} = \omega_{\text{IMU},y}^b - \hat{b}_{\text{gyro},y}^b$, compared to using roll and roll rate as in the cited works. The algorithm is deduced by exploiting that pitch is mainly affected by the wave-induced motion such that one can write

$$\begin{pmatrix} \dot{\theta} \\ \dot{q} \end{pmatrix} = \begin{pmatrix} 0 & 1 \\ -\omega_e^2 & -2\lambda_w \omega_e \end{pmatrix} \begin{pmatrix} \theta \\ q \end{pmatrix} + \begin{pmatrix} w_\theta \\ w_q \end{pmatrix}, \qquad (55)$$

where $w_\star$ represents independent white noise processes. In order to estimate λ_w (and ω_e) online, first forward Euler discretization is applied with step length T_s such that

$$\begin{pmatrix} \theta[k+1] \\ q[k+1] \end{pmatrix} = \begin{pmatrix} 1 & T_s \\ -\omega_e^2 T_s & 1 - 2\lambda_w \omega_e T_s \end{pmatrix} \begin{pmatrix} \theta[k] \\ q[k] \end{pmatrix} + \begin{pmatrix} w_\theta[k] \\ w_q[k] \end{pmatrix}. \qquad (56)$$

Furthermore, by writing the system like

$$\begin{pmatrix} \theta[k+1] \\ q[k+1] \end{pmatrix} = \begin{pmatrix} \varphi_{11} & \varphi_{12} \\ \varphi_{21} & \varphi_{22} \end{pmatrix} \begin{pmatrix} \theta[k] \\ q[k] \end{pmatrix}, \qquad (57)$$

where $\varphi_{jl}, j, l \in [1, 2]$ are unknown parameters, one can reformulate the estimation problem of (56) to estimate λ_w and ω_e indirectly. By defining a new state vector, $\boldsymbol{\varphi} := (\varphi_{11}; \varphi_{12}; \varphi_{21}; \varphi_{22})$, and assuming that φ_{jl} are constant or slowly varying ($\dot{\boldsymbol{\varphi}} = \boldsymbol{0}$ or $\dot{\boldsymbol{\varphi}} \approx \boldsymbol{0}$), the following estimation problem is obtained

$$\boldsymbol{\varphi}[k+1] = \boldsymbol{\varphi}[k], \qquad (58)$$
$$\begin{pmatrix} \theta[k] \\ q[k] \end{pmatrix} = \boldsymbol{\Lambda}[k]\boldsymbol{\varphi}[k] + \begin{pmatrix} w_\theta[k] \\ w_q[k] \end{pmatrix}, \qquad (59)$$

with

$$\boldsymbol{\Lambda}[k] = \begin{pmatrix} \theta[k-1] & q[k-1] & 0 & 0 \\ 0 & 0 & \theta[k-1] & q[k-1] \end{pmatrix}. \qquad (60)$$

Now, by defining the measurement vector

$$\boldsymbol{y}_\varphi[k] := \begin{pmatrix} \theta[k] \\ q[k] \end{pmatrix}, \qquad (61)$$

and the measurement matrix

$$\boldsymbol{C}_\varphi[k] := \boldsymbol{\Lambda}[k], \qquad (62)$$

$\boldsymbol{\varphi}[k]$ can be estimated with the discrete-time KF

$$\boldsymbol{K}_\varphi = \bar{\boldsymbol{P}}_\varphi[k]\boldsymbol{C}_\varphi^\intercal[k]\left(\boldsymbol{C}_\varphi[k]\bar{\boldsymbol{P}}_\varphi[k]\boldsymbol{C}_\varphi^\intercal[k] + \boldsymbol{R}_\varphi[k]\right)^{-1}, \quad (63a)$$
$$\hat{\boldsymbol{\varphi}}[k] = \bar{\boldsymbol{\varphi}}[k] + \boldsymbol{K}_\varphi\left(\boldsymbol{y}_\varphi[k] - \boldsymbol{C}_\varphi[k]\right), \qquad (63b)$$
$$\boldsymbol{M}_\varphi[k] = \boldsymbol{I}_4 - \boldsymbol{K}_\varphi[k]\boldsymbol{C}_\varphi[k], \qquad (63c)$$
$$\hat{\boldsymbol{P}}_\varphi[k] = \boldsymbol{M}_\varphi[k]\bar{\boldsymbol{P}}_\varphi[k]\boldsymbol{M}_\varphi[k]^\intercal + \boldsymbol{K}_\varphi \boldsymbol{R}_\varphi \boldsymbol{K}_\varphi^\intercal[k], \qquad (63d)$$
$$\bar{\boldsymbol{\varphi}}[k+1] = \hat{\boldsymbol{\varphi}}[k], \qquad (63e)$$
$$\bar{\boldsymbol{P}}_\varphi[k+1] = \hat{\boldsymbol{P}}_\varphi[k] + \boldsymbol{Q}_\varphi[k]. \qquad (63f)$$

For each k, $\hat{\omega}_e[k]$ and $\hat{\lambda}_w[k]$ are obtained with

$$\hat{\omega}_e[k] = \sqrt{-\frac{\hat{\varphi}_{21}[k]}{\hat{\varphi}_{12}[k]}}, \quad \hat{\lambda}_w[k] = \frac{\hat{\varphi}_{11}[k] - \hat{\varphi}_{22}[k]}{2\sqrt{-\hat{\varphi}_{12}[k]\hat{\varphi}_{21}[k]}}, \quad (64)$$

or

$$\hat{\omega}_e[k] = \sqrt{-\frac{\hat{\varphi}_{21}[k]}{T_s}}, \quad \hat{\lambda}_w[k] = \frac{1 - \hat{\varphi}_{22}[k]}{2\hat{\omega}_e[k]T_s}, \quad (65)$$

by exploiting how (59) relates to (56). In this study $T_s = 0.2$ s was chosen. Since neither $\hat{\omega}_e[k]$ nor $\hat{\lambda}_w[k]$ are states, the possibility of negative square-roots of the output (64)–(65) can be solved without projection algorithms. This can be done by choosing predefined minimum values of $\hat{\omega}_e[k]$ or $\hat{\lambda}_w[k]$ if the evaluation of (64)–(65) yields an imaginary result, at a certain k, in the transient phase.

4.3. Estimation of ω_e based on fast Fourier transform (FFT)

The encounter frequency $\omega_e(t)$ may also be estimated using a window of data to estimate the power spectral destiny (PSD). By choosing a window of some frequency dependent data, the estimate of $\omega_e(t)$ may be chosen as the peak frequency of the PSD. In this work the PSD calculations were based on a 15 minute window of the estimated pitch, with five minutes of overlapping data, while applying Welch's method (Welch, 1967) in doing so. However, approaches like this are dependent on historic data and are not necessarily adequately capturing transient frequency changes in the wave-induced motion. Perez (2005, Ch. 12.6) state that the sea state can typically be considered stationary for about 20 minutes. Hence, if the window length is chosen in the vicinity of 20 minutes (or shorter), FFT-based estimation of $\omega_e(t)$ may be sufficient to capture transient effects.

5. Simulation study

For evaluation of the proposed observer structure and to perform a comparison study relative the preceding observer of Bryne et al. (2015), Monte Carlo (MC) simulations of a supply ship employing DP were conducted. The observers were evaluated in three different sea states with 250 runs, each with a 50 Hz integration frequency. The MSS toolbox (Fossen and Perez, 2010) was used to generate the ship data. The JON-SWAP Spectrum, (Fossen, 2011, Ch. 8.2.1) was chosen to generate the wave-induced ship motions with the sea state parameters of Tab. 1 and the peak-shaping parameter $\gamma = 3.3$ in all three cases. For all simulations the rate gyro bias was chosen to $\boldsymbol{b}_{\text{gyro}}^b = (-0.04, 0.06, -0.05)^{\mathsf{T}}$. The statistical parameters associated with the sensor noise are presented in Tab. 2. The inertial sensors parameters are in compliance with the datasheet of the ADIS16485 IMU from Analog Devises with RMS noise of 0.067 mg/$\sqrt{\text{Hz}}$ for the accelerometers and 0.0066 °/$\sqrt{\text{Hz}}$ for the rate gyros. For positioning, the parameters were chosen in compliance with Mohleji and Wang (2010), appropriate for differential corrected GNSS (dGNSS).

Table 1: Sea State Parameters Using the Jonswap Spectrum

Sea state	Significant wave height H_s	Peak frequency ω_0 of wave spectrum
Slight	1 m	0.9 rad/s
Moderate	2.5 m	0.75 rad/s
High	7 m	0.6 rad/s

Table 2: Sensor Parameters

Sensor	Gaussian White Noise Std.	Gauss-Markov (Time cont./ driving noise std.)
Acc.	0.0046[a] m/s^2	–
Rate gyro	0.0467[a] °/s	–
dGNSS	–	$8 \cdot 60$ s/1.2 m
Compass	0.1118[b] °	600 s/$\frac{0.5°}{\cos(\mu)}$

[a] Calculated at 50 Hz.
[b] Calculated at 5 Hz ($0.05 \cdot \sqrt{5}°$ RMS).

The observers were implemented in direct form with exact discretization similar to Bryne et al. (2017) at 50 Hz. On the other hand, the measurement corrections associated with the simulated dGNSS, VVR, compass and accelerometer readings, were carried out at 1, 5, 5 and 50 Hz, respectively.

The chosen tuning for the attitude observer, in feedback-interconnection with both TMOs, that of this work and that of Bryne et al. (2015), for all three sea states was $k_1 = 0.3$, $k_2 = 0.1$ and $k_I = 0.008$. Both the presented and the preceding TMO was tuned in discrete time with

$$\boldsymbol{R}_k = \text{blokdiag}\left(\sigma_{y_k,\text{VVR}}^2, 2.4^2, 2.4^2\right),$$

while for the process noise of the presented TMO was based on the continuous-time parameters

$$\boldsymbol{Q}(t) = \text{blockdiag}\left(\sigma_{\text{acc}}^2 \cdot \boldsymbol{I}_3, \sigma_{\text{acc}}^2 \cdot \boldsymbol{S}, Q_{\text{VVR}}\right),$$
$$\boldsymbol{S} = \text{blockdiag}(S_x, S_y, S_z)$$
$$= \text{blockdiag}(1.5, 1.5, 0.1),$$
$$Q_{\text{VVR}} = 1$$
$$\sigma_{b,\text{VVR}} = 0.6,$$

and where $\boldsymbol{A}(t)$, $\boldsymbol{G}(t)$ and step length $T_s = 1/Hz$ where used to calculate $\boldsymbol{Q}_k$, the discrete-time equivalent of $\boldsymbol{G}(t)\boldsymbol{Q}(t)\boldsymbol{G}^{\mathsf{T}}(t)$, using vanLoan's method (van Loan, 1978). The preceding observer was tuned with

$$\boldsymbol{Q}(t) = \text{blockdiag}\left(\sigma_{\text{acc}}^2 \cdot \boldsymbol{I}_3, \sigma_{\text{acc}}^2 \cdot \boldsymbol{S}\right).$$

$\sigma_{b,\text{VVR}}$ is a design parameter and is a measure of the uncertainty in the knowledge of the model parameters ω_e and λ_w and the model (18)–(19) it self. The covariance tuning parameter, $R_{k,\text{VVR}} = \sigma_{y_k,\text{VVR}}^2$, associated with the VVR measurements was chosen based on

$$\sigma_{y_k,\text{VVR}} = \sigma_{y,\text{VVR}} \cdot \frac{1}{\sqrt{1/Hz}}$$

8

for the proposed observer, while using the more ad hoc formula

$$\sigma_{y_k,\text{VVR}} = \sigma_{y,\text{VVR}} \cdot \sqrt{\frac{S_z}{1/Hz}}$$

for the preceding observer. The latter choice was motivated by the desire to adjust the VVR corrections depending on the level of the driving noise, associated with estimating f_{ib}^t, in order to scale R_k dependent on the chosen Q_k. This was done to maintain an appropriate ratio between R_k and Q_k in order to ad hoc compensate for the short-term inaccuracy of the VVR since this is not taken into account in the preceding TMO.

The ad hoc choice of Q_k, using S, was done in order to tune the heave performance almost interdependent of the tuning associated with the horizontal position due to the (usually) small roll and pitch angles of a marine vessel. For the proposed observer $\sigma_{y,\text{VVR}} = 0.0005$ was chosen, where the low value was motivated due to zero noise of the VVR. For the preceding observer $\sigma_{y,\text{VVR}}$ was chosen ad hoc, $\sigma_{y,\text{VVR}} = 2.15$, yielding fair results in the slight and moderate seas since these are more common than the higher sea states (the worldwide probability of moderate sea state or lower is at 83.13 per cent, (Fossen, 2011, Ch. 8.2.1)). Moreover, $\sigma_{y,\text{VVR}}$ is a suboptimal tuning parameter when applying the observer of Bryne et al. (2015) since it will be sea state dependent, implying that gain-scheduled tuning is preferable. This, however, is not simple to perform since such tuning preferably would be based on the heave amplitude, which again is directly affected by the chosen tuning creating a loop since re-tuning will affect the heave estimates directly. An alternative would be to develop tuning rules linked to the pitch amplitude due to the kinematic heave-pitch coupling. The benefit of the newly proposed algorithm is that it implicitly re-tunes the observer based on the time-varying A-matrix. This is due to the online update of $\omega_e(t)$ and $\lambda_w(t)$ in the VVR's error model, which again affects the gain through (47). In every scenario, for both TMOs, $\vartheta = 1$ was chosen.

The statistics obtained from the MC simulations are generated based on 5 Hz evaluation of the last 90 minutes of each simulation run. The performance metrics applied are mean estimation error, RMS estimation error

$$RMS = \sqrt{\frac{1}{N}\sum_{k=1}^{N}(x_k - \hat{x}_k)^2}, \qquad (66)$$

and cumulative absolute estimation error (CAEE)

$$CAEE = \sum_{k=1}^{N}|x_k - \hat{x}_k|. \qquad (67)$$

The resulting statistics are presented in Tabs. 3–5. It is seen that performance of the heave estimation is improved approximately, 26.4, 62.3 and 72.1 percent w.r.t. RMS error, in the slight, moderate and high sea state, respectively, using the presented NLO structure including the VVR error model, compared to the observer of Bryne et al. (2015). The presented algorithm also achieves the industry standard specification of "the five cm or five per cent" RMS error in all three sea states.

Table 3: Monte Carlo statistics obtained in slight sea state

Bryne et al. (2015)	Roll	Pitch	Heave
Avg. mean error	$-2.1 \cdot 10^{-5\circ}$	$3.0 \cdot 10^{-5\circ}$	-0.0515 cm
Avg. RMS error	$0.0366°$	$0.0370°$	1.8668^a cm
Avg. CAEE	$789.3°$	$798.5°$	402.4 m
Proposed Observer	**Roll**	**Pitch**	**Heave**
Avg. mean error	$-2.5 \cdot 10^{-5\circ}$	$-2.2 \cdot 10^{-6\circ}$	-0.0480 cm
Avg. RMS error	$0.0368°$	$0.0371°$	1.3741^a cm
Avg. CAEE	$794.1°$	$801.9°$	296.2 m

[a] 5% RMS error margin: 0.92 cm.

Table 4: Monte Carlo statistics obtained in moderate sea state state

Bryne et al. (2015)	Roll	Pitch	Heave
Avg. mean error	$-1.6 \cdot 10^{-4\circ}$	$-4.0 \cdot 10^{-4\circ}$	-0.3218 cm
Avg. RMS error	$0.0382°$	$0.0374°$	5.1349^a cm
Avg. CAEE	$824.8°$	$807.0°$	$1,105.2$ m
Proposed Observer	**Roll**	**Pitch**	**Heave**
Avg. mean error	$-2.5 \cdot 10^{-4\circ}$	$-3.9 \cdot 10^{-4\circ}$	-0.3217 cm
Avg. RMS error	$0.0383°$	$0.0374°$	1.9341^a cm
Avg. CAEE	$825.3°$	$806.7°$	416.3 m

[a] 5% RMS error margin: 2.65 cm.

Regarding the attitude, the statistics indicate that the two algorithms are practically identical in performance with the chosen tuning.

The performance of the three wave-frequency estimators is illustrated in Fig. 3. One can observe that the FFT-based estimator of $\omega_e(t)$ proved to be the most robust in detecting the peak-frequency of the wave spectra in DP (where $\omega_e = \omega_0$ due to zero vessel speed). The reason for the two other estimators being slightly biased to the higher end of the spectrum might be understood from Fig. 4, showing the estimated PSD of the last 90 minutes of data from one of the MC simulations runs of the vessel in moderate sea state, based on both the heave reference and the estimated pitch, depicted in blue and red, respectively. One can observe that both signals also had one frequency component around 0.8 rad/s and one slightly above 0.8 rad/s being almost as dominant as the peak-frequency of $\omega_0 = 0.75$ of the simulated wave spectrum. One of these are probably tracked by the wave frequency estimators of Sec. 4.1–4.2. This reasoning stems from the fact that both algorithm are intrinsically based on single-frequency identification. Moreover, from Fig. 3b one

Table 5: Monte Carlo statistics obtained in high sea state

Bryne et al. (2015)	Roll	Pitch	Heave
Avg. mean error	$0.0013°$	$-0.0535°$	-2.7377 cm
Avg. RMS error	$0.0686°$	$0.0874°$	23.9277^{a} cm
Avg. CAEE	$1,484.9°$	$1,685.7°$	$5,128.8$ m
Proposed Observer	Roll	Pitch	Heave
Avg. mean error	$2.5 \cdot 10^{-4°}$	$-0.0365°$	-2.6902 cm
Avg. RMS error	$0.0688°$	$0.0662°$	6.6656^{a} cm
Avg. CAEE	$1,489.1°$	$1,318.3°$	$1,394.1$ m

[a] 5% RMS error margin: 7.78 cm.

(a) Estimate of $\omega_e(t)$.
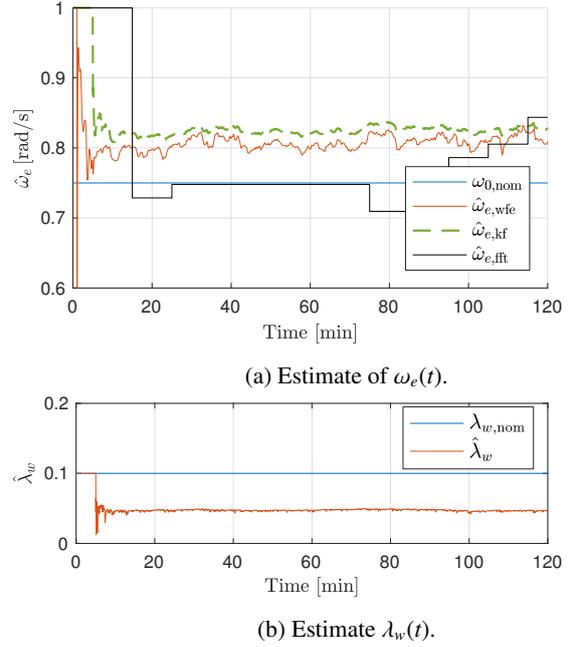

(b) Estimate $\lambda_w(t)$.

Figure 3: Wave-induced motion parameter estimates in moderate sea state.

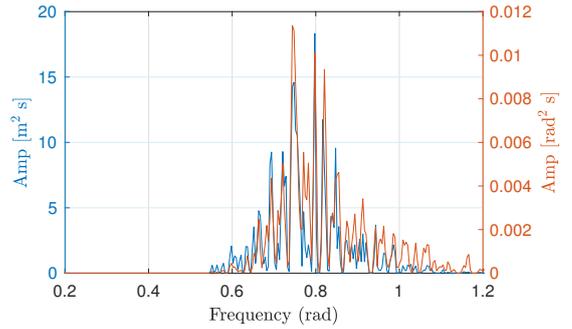Figure 4: PSD of pitch estimate (red) relative the PSD of the true heave (blue) in moderate sea state.

can see that the stationary value of $\hat{\lambda}_w$ is quite far from the recommended value of 0.1 by (Fossen, 2011, Ch. 8.2.1), indicating that the relative damping factor of the wave-induced motion should not necessarily be chosen to that of the wave spectrum's own damping factor.

A summary of the simulation study is that the attitude estimation performance of the observer proposed is equal to the preceding observer, while the heave estimation performance is increased significantly. The performance improvement is most apparent in the high state. Thus, the observer proposed is robust to changing sea states with constant tuning matrices Q and R compared to the preceding observer.

6. Validation: Experimental results

The NLO structure from Sec. 3 is further validated using data obtained from an ADIS16485 MEMS IMU from Analog Devices installed on an operational offshore vessel, owned and operated by Farstad Shipping. The data was gathered in the Norwegian Sea. The IMU was interfaced at 1000 Hz, aided by VVR, dGNSS, and gyrocompass measurements. Of the data gathered, two data sets of 119 minutes are used in the validation. The data is of two different operations, illustrated in Fig. 5, depicting the vessel tracks. One is of the offshore vessel entering DP and then performing stationkeeping, while the other is of the vessel during maneuvering.

The attitude observer and TMO was implemented at 1000 Hz. The NLO structure from Sec. 3 was validated using the same measurement-correction rates as in the simulation case study. The observers were tuned similar to that of the simulation study. Also for the validation, the encounter frequency was estimated using the FFT-based method, presented in Sec. 4.3, using the same 15 minutes of estimated pitch data with a five minute overlap from the previous window. The roll, pitch and heave estimates are compared to the solution provided by the onboard industry standard vertical reference unit (VRU). The VRU specifications are presented in Tab. 6.

6.1. Validation in DP

The statistics of the estimation performance in DP are shown in Tab. 7. Furthermore, in Fig. 8a one can observe that the three methods for obtaining $\omega_e(t)$ differ from each other, and that the FFT-based method is the one that is the best in estimating ω_e compared to the reference $\omega_{0,nom}$, obtained using FFT of the heave signal from the VRU using the entire data set of 119 minutes. The reason for the discrepancy in the methods can be understood from the Fig. 9, presenting the estimated PSD using Welch's method (Welch, 1967) of the estimated pitch compared to that of the VRU heave reference where the PSD of the estiamted pitch have two peaks just low of 0.8 rad/s. It seems that the wave frequency estimator of Sec. 4.1 converges to a frequency in this area. Nevertheless, one can see that the main peak of the estimated pitch and the heave reference signal coincides indicating that the FFT-based estimation of $\omega_e(t)$, based on pitch, in aiding the heave estimation have merit.

From the statistics one can read that the performance of the roll estimation is better than that of the pitch compared to the
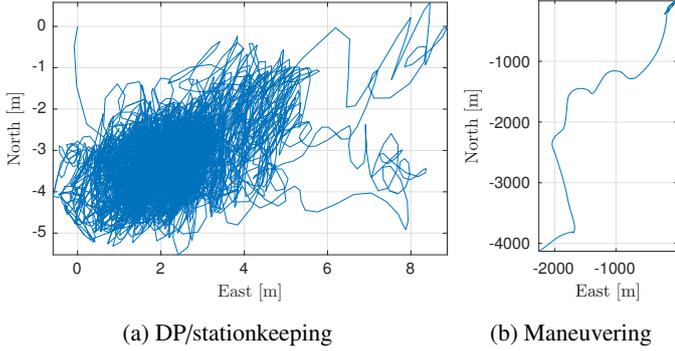
Figure 5: Track of two operations conducted in the Norwegian Sea. Path track is obtained from the onboard dGNSS.

Figure 6: Stationkeeping: Attitude estimation error.

Table 6: VRU Specification

	Static Roll & Pitch	Dynamic[a] Roll & Pitch	Heave[b]
RMS error	$0.02°$	$0.02°$	5 cm or 5 %

[a] For a sinusoidal amplitude of $\pm 5°$.
[b] Whichever is higher.
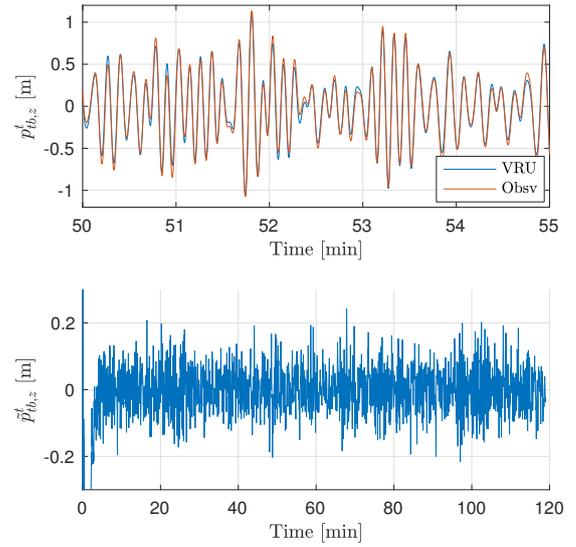
Figure 7: Stationkeeping: Heave estimates.

VRU. As with the simulation study, the proposed observer and the preceding observer provides similar results. Furthermore, the data of the two operations are gathered 45 hours and 49 minutes apart. The accelerometer bias compensation was carried out three days before the end of the last data set, indicating that the applied approach is sufficient for attitude estimation. Regarding the heave estimation, the proposed observer provided a heave estimate two per cent closer to the heave signal from the onboard VRU compared to the preceding observer. This is not close to the numbers obtained in the MC simulation. However, distinct conclusions are hard to draw since a comparison to ground truth was not carried out, but to a black-box containing its own estimator. In addition, the exact relative latency between the IMU data and the onboard VRU output was not known. Thus, an absolute comparison of the validation results relative the MC simulations is difficult to perform.

Table 7: Statistics obtained based on data gathered during DP in the Norwegian Sea.

	Roll	Pitch	Heave
Mean error	$-1.3 \cdot 10^{-4}°$	$0.0053°$	0.1461 cm
RMS error	$0.0923^{a}°$	$0.1274^{a}°$	$6.1489^{a,b}$ cm
CAEE	$1,982.8°$	$2,667.7°$	$1,305.3$ m

[a] RMS error using Bryne et al. (2015):
Roll $0.0919°$, pitch $0.1274°$, heave 6.2736 cm.
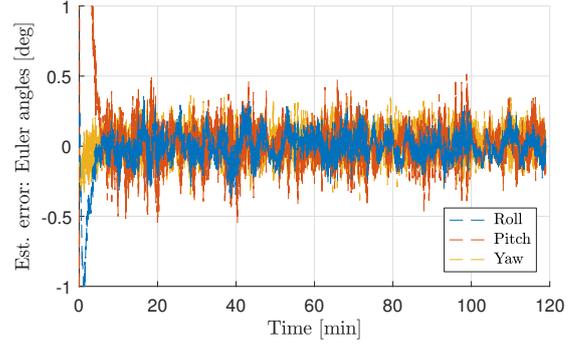[b] 5% RMS error margin: 2.1724 cm.

6.2. Validation during maneuvering

The statistics of the estimation performance obtained during maneuvering are shown in Tab. 8. Also here one can read from the statistics that both observer structures provide attitude estimates of similar error. However, the heave estimates obtained with the TMO proposed here have 15.7 per cent less RMS error relative the VRU compared to that obtained with the preceding observer. The heave estimates and the VRU heave output can be seen in Fig. 10. Furthermore, the estimates of $\omega_e(t)$ and $\lambda_w(t)$ can be observed in Fig. 11. The nominal encounter frequency $\omega_{e,\text{nom}}$ is slotwise calculated using the heave reference signal from the VRU to obtain some benchmark value when the vessel moves with forward velocity in the south-west direction as seen in Fig. 5b. In this scenario the FFT-based algorithm had the marginally better performance except between 25 and 35 minutes where the two other algorithms provided outputs closer to the peak frequency of the heave reference signal. Furthermore, from the output of the time-domain algorithms one can clearly observe the slowly-varying change in the encounter frequency. The increase of $\hat{\omega}_e(t)$ observed in Fig. 11, together with the information in Fig. 12, indicate some degree of following seas.

11
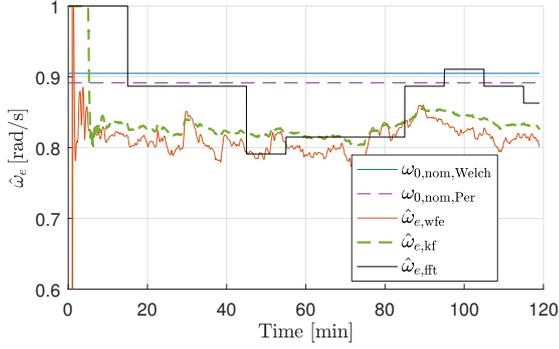
(a) Estimate of $\omega_e(t)$.
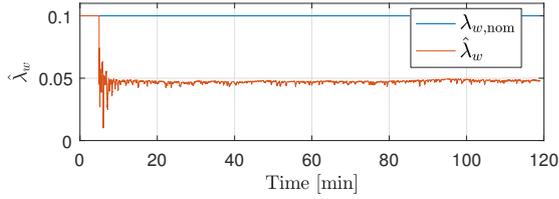
(b) Estimate $\lambda_w(t)$.

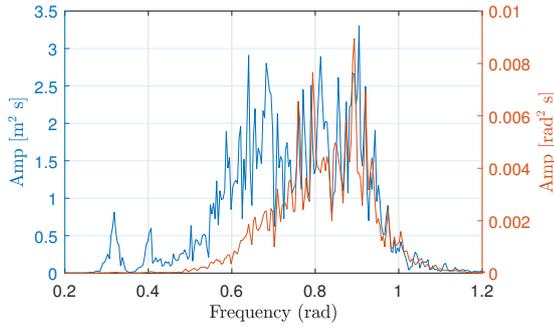Figure 8: Stationkeeping: Wave-induced motion parameter estimates.

Figure 9: Stationkeeping: PSD of estimated pitch (red) compared to the PSD of the VRUs heave refence signal.

6.3. Discussion

Since a comparison to absolute truth was not carried out there may be situations where the proposed solution is more accurate than the VRU's estimates. Moreover, one can further observe that the spectrum of the heave reference signal is quite wide, indicating that the wave-induced motion in heave is quite far from being represented by a pure sinusoidal motion, which often VRU-performance tests are subjected to.

7. Concluding remarks

Obtaining high-quality motion data of a marine vessel is both beneficial and a necessity in order to successfully and safely execute marine operations, oceanographic observations and transportation at sea. In this article six-degree-of-freedom vessel motions were estimated using a MEMS-based strapdown inertial navigation system, applying nonlinear theory, specifically tailored for marine surface vessels. The inertial navigation system was aided by differential corrected global navigation satellite system, compass and virtual vertical reference measure-

Table 8: Statistics obtained based on data gathered during maneuvering in the Norwegian Sea

	Roll	Pitch	Heave
Mean error	$-0.0023°$	$-0.0246°$	0.2047 cm
RMS error	0.1183 [a]°	0.1489 [a]°	5.0210 [a,b] cm
CAEE	$2,368.9°$	$3,095.9°$	$1,074.8$ m

[a] RMS error using Bryne et al. (2015):
Roll 0.1180°, pitch 0.1489°, heave 5.9561 cm.
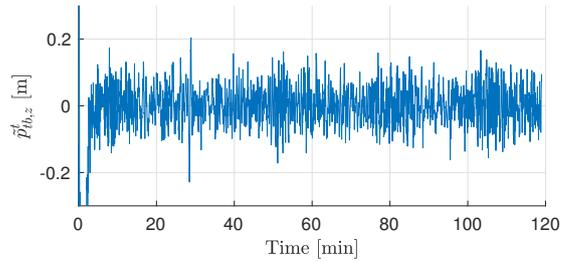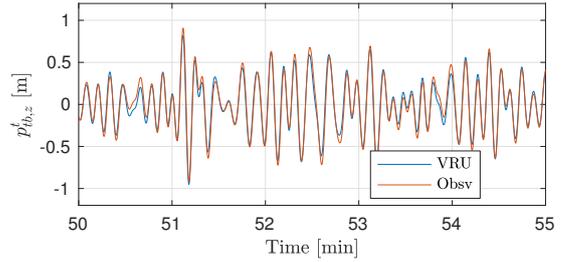[b] 5% RMS error margin: 2.0311 cm.
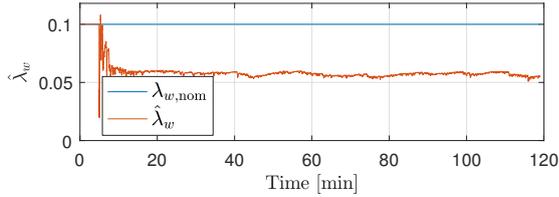

Figure 10: Maneuvering: Heave estimates.

ments. This included the introduction of an error model in addition to using the virtual vertical reference measurement as aid for the vertical axes of the INS. Moreover, the model parameters were updated online.

The origin of the observer's error dynamics was proven to be uniformly semiglobal exponentially stable. The performance of the observer's attitude and heave estimates were evaluated using Monte Carlo simulations and validated, using data collected at sea, by comparing the observer outputs' with outputs from an industry standard vertical reference unit. The results obtained are in compliance with industry standard specifications related to roll, pitch and heave estimation error. The heave estimation is improved with respect to one state-of-the-art six-degree-of-freedom estimator. In addition, both simulation and experimental results indicate online update of the error model is preferable compared to using fixed model parameters.

Further work could possible go into a in-depth study on the estimation of the relative damping factor, λ_w, in the applied error model. Even though the results from the simulation study indicate that the algorithm used shows promise, both the simulation study and the experimental validation indicate some discrepancies in estimation of the encounter frequency compared to the global exponentially stable algorithm of Belleter et al. (2015), which may indicate that also the estimate of λ_w could
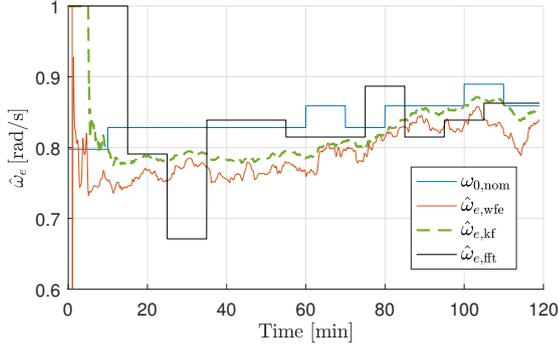
(a) Estimate of $\omega_e(t)$.

(b) Estimate $\lambda_w(t)$.
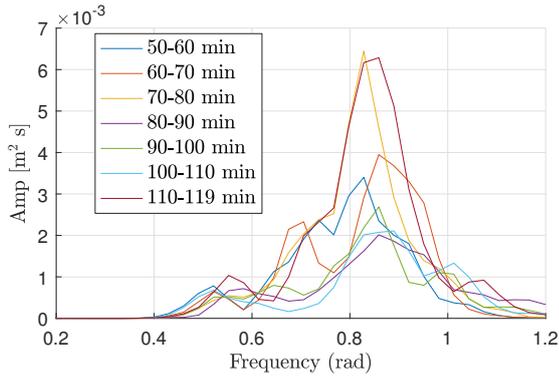
Figure 11: Maneuvering: Wave-induced motion parameter estimates.

Figure 12: Maneuvering: Slotwise PSD calculation of the heave reference signal. Peaks indicate the nominal encounter frequency $\omega_{e,\mathrm{nom}}$.

be improved. Also an investigation on how to more accurately capture the wave-induced motion in the observer may be desirable in order to improve the performance of the proposed design even more.

Acknowledgments

Appendix A. Proof of Lemma 1

PROOF. Let $\boldsymbol{Z} \in \mathbb{R}^{m \times (m-k)}$ be the matrix forming an orthonormal basis for the null space of $\boldsymbol{C}$ where m is the dimension of $\boldsymbol{A}(t)$ and $k = \mathrm{rank}(\boldsymbol{C})$ such that $\boldsymbol{CZ} = \boldsymbol{0}_{3 \times m-k}$. Considering the vector $\boldsymbol{z} = (z_1; \boldsymbol{z}_2; z_3; \boldsymbol{z}_4; \boldsymbol{z}_5; z_6; z_7)$ where $z_1, z_3, z_6, z_7 \in \mathbb{R}^1$, $\boldsymbol{z}_2 \in \mathbb{R}^2$ and $\boldsymbol{z}_4, \boldsymbol{z}_5 \in \mathbb{R}^3$, the vector $\boldsymbol{z}$ belongs to the null space of $\boldsymbol{C}$ if $\boldsymbol{Cz} = \boldsymbol{0}_{3 \times 1}$. This is valid for $z_1 = z_7 = 0$ and $\boldsymbol{z}_2 = \boldsymbol{0}_{2 \times 1}$. z_3, $\boldsymbol{z}_4$ and $\boldsymbol{z}_5$ can be arbitrary.

By considering singular value decomposition of $\boldsymbol{C} = \boldsymbol{U\Sigma V}^{\mathsf{T}}$, where $\boldsymbol{C}^{\dagger} = \boldsymbol{V\Sigma}^{\dagger}\boldsymbol{U}^{\mathsf{T}}$ and the characterization of the null space of $\boldsymbol{C}$, one obtains

$$\boldsymbol{C}^{\dagger}\boldsymbol{C} = \boldsymbol{V\Sigma}^{\dagger}\boldsymbol{\Sigma V}^{\mathsf{T}} = \begin{pmatrix} \boldsymbol{Z}_{11} & \boldsymbol{Z}_{12}^{\mathsf{T}} \\ \boldsymbol{Z}_{12} & \boldsymbol{Z}_{22} \end{pmatrix}, \qquad (\mathrm{A.1})$$

since $\boldsymbol{U}^{\mathsf{T}} = \boldsymbol{U}^{-1}$, such that $\boldsymbol{U}^{\mathsf{T}}\boldsymbol{U} = \boldsymbol{I}_3$, (Horn and Johnson, 2013, Ch. 2.1) and where

$$\boldsymbol{Z}_{11} = \mathrm{blockdiag}\left(\frac{1}{2}, \boldsymbol{Z}_p, \boldsymbol{0}_{3 \times 3}, \boldsymbol{0}_{3 \times 3}\right),$$

$$\boldsymbol{Z}_{12} = \begin{pmatrix} 0 & \boldsymbol{0}_{1 \times 9} \\ \frac{1}{2} & \boldsymbol{0}_{1 \times 9} \end{pmatrix}, \quad \boldsymbol{Z}_{22} = \begin{pmatrix} 0 & 0 \\ 0 & \frac{1}{2} \end{pmatrix},$$

and $\boldsymbol{Z}_p = \mathrm{blockdiag}(\boldsymbol{I}_2, 0)$. Then

$$\boldsymbol{L}_{\vartheta}\boldsymbol{C}^{\dagger}\boldsymbol{C} = \boldsymbol{C}^{\dagger}\boldsymbol{C}\boldsymbol{L}_{\vartheta}, \qquad (\mathrm{A.2})$$

is achieved due to the structure of $\boldsymbol{C}^{\dagger}\boldsymbol{C}$ and since $\boldsymbol{L}_{\vartheta}$ is diagonal and has 1 in the upper left and bottom right element such that $1/2$ contained in $\boldsymbol{Z}_{12}$ is distributed equivalent in both sides of (A.2) in the upper and lower, left and right elements, respectively. Then the result follows by $\boldsymbol{E}_{\vartheta}$ post-multiplied with $\boldsymbol{C}$, using (A.2) and $\boldsymbol{CC}^{\dagger}\boldsymbol{C} = \boldsymbol{C}$ (Horn and Johnson, 2013, Ch. 7.3) such that $\boldsymbol{E}_{\vartheta}\boldsymbol{C} = \boldsymbol{CL}_{\vartheta}\boldsymbol{C}^{\dagger}\boldsymbol{C} = \boldsymbol{CC}^{\dagger}\boldsymbol{CL}_{\vartheta} = \boldsymbol{CL}_{\vartheta}$.

$\square$

Appendix B. Proof of Lemma 2

PROOF. UCO of the LTV system $\left(\boldsymbol{A}(t), \boldsymbol{R}^{-1/2}(t)\boldsymbol{C}\right)$ can be established with the observability Gramian

$$\boldsymbol{\mathcal{W}}_o(t_0, t_1) = \int_{t_0}^{t_1} \boldsymbol{\Phi}^{\mathsf{T}}(t_0, \tau)\boldsymbol{C}^{\mathsf{T}}\boldsymbol{R}^{-1}\boldsymbol{C}\boldsymbol{\Phi}(t_0, \tau)\, \mathrm{d}\tau, \qquad (\mathrm{B.1})$$

while UCC of $\left(\boldsymbol{A}(t), \boldsymbol{Q}^{-1/2}(t)\boldsymbol{G}(t)\right)$ can be established with the controllability Gramian

$$\boldsymbol{\mathcal{W}}_c(t_0, t_1) = \int_{t_0}^{t_1} \boldsymbol{\Phi}(t_0, \tau)\boldsymbol{G}(t)\boldsymbol{Q}(t)\boldsymbol{G}^{\mathsf{T}}(t)\boldsymbol{\Phi}^{\mathsf{T}}(t_0, \tau)\, \mathrm{d}\tau, \qquad (\mathrm{B.2})$$

for all $t \geq 0$. Moreover, the system $(\boldsymbol{A}(t), \boldsymbol{G}(t), \boldsymbol{C})$ is UCO and UCC if and only if both $\boldsymbol{\mathcal{W}}_o(t_0, t_1)$ and $\boldsymbol{\mathcal{W}}_c(t_0, t_1)$ are positive definite on every interval $t \in [t_0, t_1]$ for $t_1 > t_0$ for all $t \geq 0$. In addition, the explicit time dependency of ω_e, λ_w and $\sigma_{b,\mathrm{VVR}}$ is omitted in the reminder of the proof.

The state transition matrix $\boldsymbol{\Phi}(t_0,\tau) = e^{(A(\tau-t_0))}$ takes the form of

$$\boldsymbol{\Phi}(\tau) = \begin{pmatrix} 1 & 0\ 0\ (\tau-t_0) & 0\ 0\ \frac{(\tau-t_0)^2}{2} & 0\ 0\ \frac{(\tau-t_0)^3}{6} & \mathbf{0}_{1\times2} \\ \mathbf{0}_{3\times1} & \boldsymbol{I}_3 & (\tau-t_0)\boldsymbol{I}_3 & \frac{(\tau-t_0)^2}{2}\boldsymbol{I}_3 & \mathbf{0}_{3\times2} \\ \mathbf{0}_{3\times1} & \mathbf{0}_{3\times3} & \boldsymbol{I}_3 & (\tau-t_0)\boldsymbol{I}_3 & \mathbf{0}_{3\times2} \\ \mathbf{0}_{3\times1} & \mathbf{0}_{3\times3} & \mathbf{0}_{3\times3} & \boldsymbol{I}_3 & \mathbf{0}_{3\times2} \\ \mathbf{0}_{2\times1} & \mathbf{0}_{2\times3} & \mathbf{0}_{2\times3} & \mathbf{0}_{2\times3} & e^{(\boldsymbol{F}_{\text{VVR}}(\tau-t_0))} \end{pmatrix}. \tag{B.3}$$

Moreover, due to the block-diagonal structure of $\boldsymbol{A}(t)$ one have that

$$\boldsymbol{A}^j(t) = \begin{pmatrix} \boldsymbol{A}_0^j & \mathbf{0}_{10\times2} \\ \mathbf{0}_{2\times10} & \boldsymbol{F}_{\text{VVR}}^j(t) \end{pmatrix}, \quad j \in [1, \dots m-1], \tag{B.4}$$

where m is the dimension of $\boldsymbol{A}(t)$. Therefore, one may study the observability of the subsystems $(\boldsymbol{A}_0, \boldsymbol{C}_0)$, with dimension $m_0 = 10$, and $(\boldsymbol{F}_{\text{VVR}}(t), \boldsymbol{H}_{\text{VVR}})$, with dimension $l = 2$, separately. By considering the nominal linear-time invariant (LTI) system $(\boldsymbol{A}_0, \boldsymbol{C}_0)$, applying the rank condition on $\mathcal{O}_0 = \left(\boldsymbol{C}_0; \boldsymbol{C}_0\boldsymbol{A}_0; \boldsymbol{C}_0\boldsymbol{A}_0^2; \dots; \boldsymbol{C}_0\boldsymbol{A}_0^{m_0-1}\right)$ is trivial, and yields rank m_0. Then if the system $(\boldsymbol{F}_{\text{VVR}}(t), \boldsymbol{H}_{\text{VVR}})$ is UCO, the complete system $(\boldsymbol{A}(t), \boldsymbol{C})$ is UCO. Now, the observability Gramian related to the lower right block of $(\boldsymbol{A}(t), \boldsymbol{C})$ is considered,

$$\mathcal{W}_{o_{\text{VVR}}}(t_0,t_1) = \int_{t_0}^{t_1} \boldsymbol{\Upsilon}_{o_{\text{VVR}}}^{\mathsf{T}}(t_0,\tau) R_{\text{VVR}}^{-1} \boldsymbol{\Upsilon}_{o_{\text{VVR}}}(t_0,\tau)\,d\tau, \tag{B.5}$$

where $\boldsymbol{\Upsilon}_{o_{\text{VVR}}}(t_0,\tau) = \boldsymbol{H}_{\text{VVR}}\boldsymbol{\Phi}_{\text{VVR}}(t_0,\tau)$. Continuing with the non-zero vector $\boldsymbol{z} = (z_1, z_2)^{\mathsf{T}} \in \mathbb{R}^l$, and pre and post multiplying (B.5) with $\boldsymbol{z}$,

$$\boldsymbol{z}^{\mathsf{T}}\mathcal{W}_{o_{\text{VVR}}}(t_0,t_1)\boldsymbol{z} = \int_{t_0}^{t_1} \boldsymbol{z}^{\mathsf{T}}\boldsymbol{\Upsilon}_{o_{\text{VVR}}}^{\mathsf{T}}(t_0,\tau) R_{\text{VVR}}^{-1} \boldsymbol{\Upsilon}_{o_{\text{VVR}}}(t_0,\tau)\boldsymbol{z}\,d\tau, \tag{B.6}$$

is obtained for all $t_1 \geq t_0$. Since R_{VVR} is a positive scalar one may write

$$\boldsymbol{z}^{\mathsf{T}}\mathcal{W}_{o_{\text{VVR}}}(t_0,t_1)\boldsymbol{z} \geq R_{\max} \int_{t_0}^{t_1} \|\boldsymbol{\Upsilon}_{o_{\text{VVR}}}(t_0,\tau)\boldsymbol{z}\|_2^2\,d\tau, \tag{B.7}$$

where $R_{\max}$ is the maximum value of R_{VVR} over the interval $[t_0, t_1]$. Then it is relatively straightforward to obtain

$$\boldsymbol{\Upsilon}_{o_{\text{VVR}}}(t_0,\tau)\boldsymbol{z} = \dots$$
$$- \frac{\omega_e e^{-\lambda_w}}{2\sqrt{\lambda_w^2-1}}\Big(e^{\sqrt{\lambda_w^2-1}\omega_e(\tau-t_0)} - e^{-\sqrt{\lambda_w^2-1}\omega_e(\tau-t_0)}\Big)z_1$$
$$+ \Big(\frac{e^{-\lambda_w}}{2}\Big(e^{\sqrt{\lambda_w^2-1}\omega_e(\tau-t_0)} + e^{-\sqrt{\lambda_w^2-1}\omega_e(\tau-t_0)}\Big)$$
$$- \frac{\lambda_w e^{-\lambda_w}}{2\sqrt{\lambda_w^2-1}}\Big(e^{\sqrt{\lambda_w^2-1}\omega_e(\tau-t_0)} - e^{-\sqrt{\lambda_w^2-1}\omega_e(\tau-t_0)}\Big)\Big)z_2. \tag{B.8}$$

Furthermore, the fact that $0 < \lambda_w < 1$ is exploited, resulting in

$$\sqrt{\lambda_w^2-1} = \sqrt{1-\lambda_w^2}\,i \tag{B.9}$$

such that (B.8) becomes

$$\boldsymbol{\Upsilon}_{o_{\text{VVR}}}(t_0,\tau)\boldsymbol{z} = \dots$$
$$- \frac{\omega_e e^{-\lambda_w}}{2i\sqrt{1-\lambda_w^2}}\Big(e^{\sqrt{1-\lambda_w^2}\omega_e(\tau-t_0)i} - e^{-\sqrt{1-\lambda_w^2}\omega_e(\tau-t_0)i}\Big)z_1$$
$$+ \Big(\frac{e^{-\lambda_w}}{2}\Big(e^{\sqrt{1-\lambda_w^2}\omega_e(\tau-t_0)i} + e^{-\sqrt{1-\lambda_w^2}\omega_e(\tau-t_0)i}\Big)$$
$$- \frac{\lambda_w e^{-\lambda_w}}{2i\sqrt{1-\lambda_w^2}}\Big(e^{\sqrt{1-\lambda_w^2}\omega_e(\tau-t_0)i} - e^{-\sqrt{1-\lambda_w^2}\omega_e(\tau-t_0)i}\Big)\Big)z_2, \tag{B.10}$$

which again can be written as

$$\boldsymbol{\Upsilon}_{o_{\text{VVR}}}(t_0,\tau)\boldsymbol{z} = z_2 e^{-\lambda_w}\cos\Big(\sqrt{1-\lambda_w^2}\omega_e(\tau-t_0)\Big)$$
$$- \frac{(\omega_e z_1 + \lambda_w z_2)e^{-\lambda_w}}{\sqrt{1-\lambda_w^2}}\sin\Big(\sqrt{1-\lambda_w^2}\omega_e(\tau-t_0)\Big). \tag{B.11}$$

It follows that $\|\boldsymbol{\Upsilon}_{o_{\text{VVR}}}(t_0,\tau)\boldsymbol{z}\|_2^2$ can be obtained as

$$\|\boldsymbol{\Upsilon}_{o_{\text{VVR}}}(t_0,\tau)\boldsymbol{z}\|_2^2 = \frac{(\omega_e z_1 + \lambda_w z_2)^2 e^{-2\lambda_w}}{1-\lambda_w^2}\sin^2(c(\tau-t_0))$$
$$- 2\frac{(\omega_e z_1 z_2 + \lambda_w z_2^2)e^{-2\lambda_w}}{\sqrt{1-\lambda_w^2}}\sin(c(\tau-t_0))\cos(c(\tau-t_0))$$
$$+ z_2^2 e^{-2\lambda_w}\cos^2(c(\tau-t_0)), \tag{B.12}$$

for $c := \sqrt{1-\lambda_w^2}\omega_e$. Now, (B.12) can be simplified further,

$$\|\boldsymbol{\Upsilon}_{o_{\text{VVR}}}(t_0,\tau)\boldsymbol{z}\|_2^2 = \frac{(\omega_e z_1 + \lambda_w z_2)^2 e^{-2\lambda_w}}{1-\lambda_w^2}\sin^2(c(\tau-t_0))$$
$$- \frac{(\omega_e z_1 z_2 + \lambda_w z_2^2)e^{-2\lambda_w}}{\sqrt{1-\lambda_w^2}}\sin(2c(\tau-t_0)) + z_2^2 e^{-2\lambda_w}\cos^2(c(\tau-t_0)). \tag{B.13}$$

From (B.13) one notice that for $\tau \geq t_0$ $\|\boldsymbol{\Upsilon}_{o_{\text{VVR}}}(t_0,\tau)\boldsymbol{z}\|_2 = 0$ if and only if $\boldsymbol{z} = \mathbf{0}_{l\times1}$. Moreover, since

$$\int_{t_0}^{t_1}\sin^2(c(\tau-t_0))\,d\tau = \frac{2c(t_1-t_0) + \sin(2c(t_0-t_1))}{4c}, \tag{B.14}$$

$$\int_{t_0}^{t_1}\cos^2(c(\tau-t_0))\,d\tau = \frac{2c(t_1-t_0) + \sin(2c(t_1-t_0))}{4c}, \tag{B.15}$$

where $2c(t_1-t_0)$ always is positive and

$$\frac{(\omega_e z_1 + \lambda_w z_2)^2 e^{-2\lambda_w}}{1-\lambda_w^2} \neq z_2^2 e^{-2\lambda_w} \quad \forall t \geq 0, \boldsymbol{z} \neq \mathbf{0}_{l\times1}, \tag{B.16}$$

result in $\boldsymbol{z}^{\mathsf{T}}\mathcal{W}_{o_{\text{VVR}}}(t_0,t_1)\boldsymbol{z}$ to be uniformly positive. Hence, for any $t_1 > t_0$, $\mathcal{W}_{o_{\text{VVR}}}(t_0,t_1)$ is positive definite (and therefore invertible), since ω_e is positive and bounded and $0 < \lambda_w < 1$ on every interval $t \in [t_0, t_1]$. Thus, $(\boldsymbol{A}(t), \boldsymbol{R}^{-1/2}\boldsymbol{C})$ is UCO.

Now, controllability is considered, making a similar argument as above. With no loss of generality, $\boldsymbol{R}(t, \hat{\boldsymbol{q}}_b^t) = \boldsymbol{I}_3$ can be assumed, for usage in $\boldsymbol{B}_0$ cf. (32), due to the rotation matrix having unit norm and rank of 3 uniformly. By considering the nominal LTI system $(\boldsymbol{A}_0, \boldsymbol{B}_0)$, applying the rank condition

on $\mathcal{C}_0 = \left(\boldsymbol{B}_0, \, \boldsymbol{A}_0 \boldsymbol{B}_0, \, \boldsymbol{A}_0^2 \boldsymbol{B}_0, \, \ldots, \, \boldsymbol{A}_0^{m_0-1} \boldsymbol{B}_0 \right)$ is trivial, and yields rank m_0. Then if the system $(\boldsymbol{F}_{\text{VVR}}(t), \boldsymbol{G}_{\text{VVR}}(t))$, is UCC, the complete system $(\boldsymbol{A}(t), \boldsymbol{G}(t))$ is UCC. Now, the controllability Gramian for the lower right block of $(\boldsymbol{A}(t), \boldsymbol{G}(t))$, is considered,

$$\mathcal{W}_{c_{\text{VVR}}}(t_0, t_1) = \int_{t_0}^{t_1} \boldsymbol{\Upsilon}_{c_{\text{VVR}}}^{\mathsf{T}}(t_0, \tau) Q_{\text{VVR}} \boldsymbol{\Upsilon}_{c_{\text{VVR}}}(t_0, \tau) \, \mathrm{d}\tau, \quad \text{(B.17)}$$

where $\boldsymbol{\Upsilon}_{c_{\text{VVR}}}(t_0, \tau) = \boldsymbol{G}_{\text{VVR}}^{\mathsf{T}} \boldsymbol{\Phi}_{\text{VVR}}^{\mathsf{T}}(t_0, \tau)$. Continuing, UCC of $(\boldsymbol{F}_{\text{VVR}}(t), \boldsymbol{G}_{\text{VVR}}(t))$ is proven by applying the non-zero vector $\boldsymbol{z} = (z_1, z_2)^{\mathsf{T}} \in \mathbb{R}^l$ similarly as above such that

$$\boldsymbol{z}^{\mathsf{T}} \mathcal{W}_{c_{\text{VVR}}}(t_0, t_1) \boldsymbol{z} = \int_{t_0}^{t_1} \boldsymbol{z}^{\mathsf{T}} \boldsymbol{\Upsilon}_{c_{\text{VVR}}}^{\mathsf{T}}(t_0, \tau) \boldsymbol{\Upsilon}_{c_{\text{VVR}}}(t_0, \tau) \boldsymbol{z} \, \mathrm{d}\tau,$$
$$= \int_{t_0}^{t_1} \| \boldsymbol{\Upsilon}_{c_{\text{VVR}}}(t_0, \tau) \boldsymbol{z} \|_2^2 \, \mathrm{d}\tau, \quad \text{(B.18)}$$

using that $Q_{\text{VVR}} = 1$, for all $t_1 \geq 0$. Then it is relatively straightforward to obtain

$$\boldsymbol{\Upsilon}_{c_{\text{VVR}}}(t_0, \tau) \boldsymbol{z} = \ldots$$
$$\frac{\sigma_{b,\text{VVR}} \mathrm{e}^{-\lambda_w}}{2\omega_e \sqrt{\lambda_w^2 - 1}} \left(\mathrm{e}^{-\sqrt{\lambda_w^2-1}\omega_e(\tau-t_0)} - \mathrm{e}^{\sqrt{\lambda_w^2-1}\omega_e(\tau-t_0)} \right) z_1$$
$$+ \left(\frac{\sigma_{b,\text{VVR}} \mathrm{e}^{-\lambda_w}}{2} \left(\mathrm{e}^{\sqrt{\lambda_w^2-1}\omega_e(\tau-t_0)} + \mathrm{e}^{-\sqrt{\lambda_w^2-1}\omega_e(\tau-t_0)} \right) \right.$$
$$\left. - \frac{\sigma_{b,\text{VVR}} \lambda_w \mathrm{e}^{-\lambda_w}}{2\sqrt{\lambda_w^2-1}} \left(\mathrm{e}^{\sqrt{\lambda_w^2-1}\omega_e(\tau-t_0)} - \mathrm{e}^{-\sqrt{\lambda_w^2-1}\omega_e(\tau-t_0)} \right) \right) z_2. \tag{B.19}$$

which is structurally similar to (B.8). By following similar steps as to (B.10)–(B.16) one can state that for any $t_1 > t_0$ $\mathcal{W}_{c_{\text{VVR}}}(t_0, t_1)$ is positive definite since ω_e and $\sigma_{b,\text{VVR}}$ is positive and bounded and $0 < \lambda_w < 1$ on every interval $[t_0, t_1]$. Thus, $(\boldsymbol{A}(t), \boldsymbol{Q}^{-1/2}(t)\boldsymbol{G}(t))$ is UCC.

$\square$

Appendix C. Proof of Lemma 3

PROOF. By considering the Lyapunov function candidate $U(t, \boldsymbol{\eta}) = \vartheta^{-1} \boldsymbol{\eta}^{\mathsf{T}} \boldsymbol{P}^{-1} \boldsymbol{\eta}$, where $\boldsymbol{P} = \boldsymbol{P}^{\mathsf{T}} > 0$ is the solution of (47), the proof follows from Kalman and Bucy (1961); Anderson (1971). Along the trajectories of (50) and (47) one obtains

$$\dot{U}(t, \boldsymbol{\eta}) = -\boldsymbol{\eta}^{\mathsf{T}} \left(\boldsymbol{P}^{-1} \boldsymbol{G} \boldsymbol{Q} \boldsymbol{G}^{\mathsf{T}} \boldsymbol{P}^{-1} + \boldsymbol{C}^{\mathsf{T}} \boldsymbol{R}^{-1} \boldsymbol{C} \right) \boldsymbol{\eta} < 0, \forall t \geq 0 \quad \text{(C.1)}$$

where $\boldsymbol{P}$ is bounded above and below due to UCO of $(\boldsymbol{A}(t), \boldsymbol{C})$, and UCC of $(\boldsymbol{A}(t), \boldsymbol{G}(t))$, for a positive definite $\boldsymbol{R}$ and $\boldsymbol{Q}$ matrices, yielding that the origin of the nominal error dynamics is GES.

$\square$

Appendix D. Proof of Proposition 1

PROOF. The proof is mainly based on the proofs of Grip et al. (2013), Bryne et al. (2014) and Johansen et al. (2017). For

completeness the main components of the proof are outlined below.

From the proof of Lemma 3 one may obtained $U(t, \boldsymbol{\eta}) = \boldsymbol{\eta}^{\mathsf{T}} \boldsymbol{\vartheta}^{-1} \boldsymbol{P}^{-1} \boldsymbol{\vartheta}^{-1} \boldsymbol{\eta}$ and that

$$\dot{U} \leq \gamma_1 \|\boldsymbol{\eta}\|_2 + \frac{1}{\vartheta} \gamma_2 \gamma_4 \|\boldsymbol{\eta}\|_2^2 + \frac{1}{\vartheta^4} \gamma_3 \gamma_4 \|\boldsymbol{\eta}\|_2 \cdot \|\boldsymbol{\chi}\|_2, \quad \text{(D.1)}$$

with

$$\frac{2}{\vartheta} \boldsymbol{\eta}^{\mathsf{T}} \boldsymbol{\vartheta}^{-1} \boldsymbol{P}^{-1} \boldsymbol{\rho}_1(t, \boldsymbol{\eta}) \leq \gamma_1 \|\boldsymbol{\eta}\|_2 \quad \text{(D.2)}$$
$$\frac{2}{\vartheta^4} \boldsymbol{\eta}^{\mathsf{T}} \boldsymbol{\vartheta}^{-1} \boldsymbol{P}^{-1} \boldsymbol{\rho}_2(t, \boldsymbol{\chi}) \leq \frac{1}{\vartheta} \gamma_2 \gamma_4 \|\boldsymbol{\eta}\|_2^2 + \frac{1}{\vartheta^4} \gamma_3 \gamma_4 \|\boldsymbol{\eta}\|_2 \cdot \|\boldsymbol{\chi}\|_2, \tag{D.3}$$

where $\gamma_1, \gamma_2, \gamma_3, \gamma_4 > 0$ are constants independent of ϑ since $\|\boldsymbol{\vartheta}^{-1}\| = 1$ for all $\vartheta \geq 1$. Moreover, since a uniform bound on $\boldsymbol{P}^{-1}$ can be established independent of ϑ, (Johansen and Fossen (2015), Lemma 6), the intermediate results of Grip et al. (2013) are utilized, where it can be shown that for any $\delta > 0$ and $T > 0$ there exist a $\vartheta_1^* \geq 1$ such that for $\vartheta \geq \vartheta_1^*$ there exist an invariant set $\mathcal{X}_1 \in \mathbb{R}^{12}$ such that for $\|\boldsymbol{\eta}(0)\|_2 \in \mathcal{X}_1$ one have that $\|\boldsymbol{\eta}\|_2 \leq \delta$, for all $t \geq T$. By further following the cited results, the function

$$W(t, \tilde{s}, \tilde{\boldsymbol{r}}, \tilde{\boldsymbol{b}}^b) := \left(1 - \tilde{s}^2 \right) + 2\ell \tilde{s} \tilde{\boldsymbol{r}} R(\boldsymbol{q}_b^t) \tilde{\boldsymbol{b}}^b + \frac{\ell}{k_I} (\tilde{\boldsymbol{b}}^b)^{\mathsf{T}} \tilde{\boldsymbol{b}}^b, \quad \text{(D.4)}$$

is defined, where ℓ is a constant taken from Grip et al. (2012a). Moreover, in Grip et al. (2013) it was shown that for $|\tilde{s}| > \bar{\epsilon}$, $\dot{W}$ satisfy,

$$\dot{W} \leq \gamma_6 \|\boldsymbol{\chi}\|_2^2 + \gamma_5 \|\boldsymbol{\chi}\|_2 \cdot \|\boldsymbol{\eta}\|_2, \quad \text{(D.5)}$$

for some constants $\gamma_5, \gamma_6 > 0$, independent of ϑ. Moreover, the Lyapunov function candidate

$$V(t, \boldsymbol{\eta}, \boldsymbol{\chi}) := U(t, \boldsymbol{\eta}) + \frac{1}{\vartheta_7} W(t, \boldsymbol{\chi}) \quad \text{(D.6)}$$

is defined, resulting in

$$\dot{V} \leq -\boldsymbol{z}^{\mathsf{T}} \boldsymbol{M}(\vartheta) \boldsymbol{z}, \quad \text{(D.7)}$$

with $\boldsymbol{z} = (\|\boldsymbol{\eta}\|_2; \|\boldsymbol{\chi}\|_2) \in \mathbb{R}^2$ and

$$\boldsymbol{M}(\vartheta) = \begin{pmatrix} \gamma_1 - \frac{\gamma_2 \gamma_4}{\vartheta} & \star \\ -\frac{\gamma_3 \gamma_4 + \gamma_5}{2\vartheta^4} & \frac{\gamma_6}{\vartheta^7} \end{pmatrix}, \quad \text{(D.8)}$$

and where $\star$ indicate symmetry. Considering the principal minors of $\boldsymbol{M}(\vartheta)$, one obtain $\boldsymbol{M}(\vartheta) > 0$ with

$$\vartheta \geq \max \left(\frac{\gamma_2 \gamma_4}{\gamma_1}, \frac{\gamma_2 \gamma_4 \gamma_6 + \frac{1}{4}(\gamma_3 \gamma_4 + \gamma_5)^2}{\gamma_1 \gamma_6} \right). \quad \text{(D.9)}$$

Thus by choosing ϑ_1^* to satisfy (D.9) and $\vartheta \geq \vartheta_1^*$ accordingly, there exist an invariant set $\mathcal{X}_2$, where for all $\tilde{\boldsymbol{x}} \in \mathcal{X}_2$ and constants $\alpha_3, \alpha_4 > 0$, such that

$$\dot{V} \leq -\alpha_3 \|\boldsymbol{z}\|_2^2 - \alpha_4 \|\boldsymbol{\chi}\|_2^2 \leq -2\beta V, \quad \text{(D.10)}$$

for some $\beta > 0$ where $\mathcal{X} \subset \mathcal{X}_1 \cap \mathcal{X}_2$ is chosen as the largest invariant set. The USGES result, applying the definition of Loria

15

and Panteley (2005), of the origin $(\tilde{x}; \chi) = 0$ then follows by applying the comparison lemma (Khalil (2002), Lemma 3.4), such that

$$V(t) \leq V(0)\mathrm{e}^{-2\beta t}, \quad \forall t \geq 0. \tag{D.11}$$

□

References

Anderson, B., 1971. Stability properties of Kalman-Bucy filters. Journal of the Franklin Institute 1 (2), 137–144.

Auestad, O. F., Gravdahl, J. T., Fossen, T. I., Sept. 17–20 2013. Heave motion estimation on a craft using a strapdown inertial measurement unit. In: Proc of the 9th IFAC Conference on Control Applications in Marine Systems. Osaka, Japan, pp. 298—303.

Belleter, D. J., Galeazzi, R., Fossen, T. I., 2015. Experimental verification of a globally exponentially stable nonlinear wave encounter frequency estimator. Ocean Engineering, Elsevier 97 (15), 48–56.

Bryne, T. H., Fossen, T. I., Johansen, T. A., June 16–19 2014. Nonlinear observer with time-varying gains for inertial navigation aided by satellite reference systems in dynamic positioning. In: Proc. of the IEEE Mediterranean Conference on Control and Automation. Palermo, Italy, pp. 1353–1360.

Bryne, T. H., Fossen, T. I., Johansen, T. A., Aug. 24–26 2015. A virtual vertical reference concept for GNSS/INS applications at the sea surface. In: Proc. of the 10th IFAC Conference on Manoeuvring and Control of Marine Craft (MCMC). Copenhagen, Denmark, pp. 127–133, received the best regular paper award at IFAC MCMC'15.

Bryne, T. H., Hansen, J. M., Rogne, R. H., Sokolova, N., Fossen, T. I., Johansen, T. A., 2017. Nonlinear observers for integrated INS/GNSS navigation – Implementation aspects. IEEE Control Systems Magazine 37 (3), 59–86.

Bryne, T. H., Rogne, R. H., Fossen, T. I., Johansen, T. A., Sept. 13–16 2016. Attitude and heave estimation for ships using MEMS-based inertial measurements. In: Proc. of the 10th IFAC Conference on Control Applications in Marine Systems (CAMS). Trondheim, pp. 568–575.

Farrell, J. A., 2008. Aided Navigation: GPS with High Rate Sensors. McGraw-Hill.

Fossen, T. I., 2011. Handbook of Marine Craft Hydrodynamics and Motion Control. John Wiley & Sons, Ltd.

Fossen, T. I., Perez, T., 2009. Kalman filtering for positioning and heading control of ships and offshore rigs. IEEE Control Systems Magazine 29 (6), 32–46.

Fossen, T. I., Perez, T., 2010. Marine Systems Simulator (MSS). Viewed 01.08.2014, www.marinecontrol.org.

Fossen, T. I., Strand, J. P., 1999. Passive nonlinear observer design for ships using lyapunov methods: full-scale experiments with a supply vessel. Automatica 35 (1), 3 – 16.

Godhavn, J.-M., 28 Sept.–1 Oct. 1998. Adaptive tuning of heave filter in motion sensor. In: OCEANS '98 Conf. Proc. Vol. 1. Nice, France, pp. 174–178.

Godhavn, J.-M., 11–14 Sept. 2000. High quality heave measurements based on GPS RTK and accelerometer technology. In: OCEANS 2000 MTS/IEEE Conference and Exhibition. Vol. 1. Providence, RI, pp. 309–314.

Grip, H. F., Fossen, T. I., Johansen, T. A., Saberi, A., 2012a. Attitude estimation using biased gyro and vector measurements with time-varying reference vectors. IEEE Transactions on Automatic Control 57 (5), 1332—1338.

Grip, H. F., Fossen, T. I., Johansen, T. A., Saberi, A., June 2013. Nonlinear observer for GNSS-aided inertial navigation with quaternion-based attitude estimation. In: Proc. of the American Contr. Conf. Washington, DC, pp. 272–279.

Grip, H. F., Saberi, A., 2010. Structural decomposition of linear multivariable systems using symbolic computations. International Journal of Control 83 (7), 1414–1426.

Grip, H. F., Saberi, A., Johansen, T. A., July 2012b. Observers for interconnected nonlinear and linear systems. Automatica 48 (7), 1339–1346.

Groves, P. D., 2013. Principles of GNSS, Inertial, and Multisensor Integrated Navigation Systems, 2nd Edition. Artech House.

Horn, R. A., Johnson, C. R., 2013. Matrix Analysis, 2nd Edition. Cambridge University Press, New York.

Hua, M.-D., Ducard, G., Hamel, T., Mahony, R., Rudin, K., 2014. Implementation of a nonlinear attitude estimator for aerial robotic vehicles. IEEE Transactions On Control System Technology 22 (1), 201–212.

Johansen, T. A., Fossen, T. I., July 15–17 2015. Nonlinear observer for inertial navigation aided by pseudo-range and range-rate measurements. In: Proc. of the European Contr. Conf. Linz, Austria, pp. 1673–1680.

Johansen, T. A., Hansen, J. M., Fossen, T. I., 2017. Nonlinear observer for tightly integrated inertial navigation aided by pseudo-range measurements. ASME Journal of Dynamic Systems, Measurement and Control 139 (1), 011007–011007–10.

Kalman, R., Bucy, R., 1961. New results in linear filtering and prediction theory. American Society of Mechanical Engineers – Transactions – Journal of Basic Engineering Series D 83 (1), 95–108.

Khalil, H. K., 2002. Nonlinear Systems, 3rd Edition. Prentice Hall.

Küchler, S., Eberharter, J. K., Langer, K., Schneider, K., Sawodny, O., 2011. Heave motion estimation of a vessel using acceleration measurements. In: Proc. of the 18th IFAC World Congress. MIlan, Italy, pp. 14742–14747.

Loria, A., Panteley, E., 2005. Cascaded nonlinear time-varying systems: Analysis and design. In: Lamnabhi-Lagarrigue, F., Loria, A., Panteley, E. (Eds.), Adv. Top. in Cntrl. Sys. Theory. Vol. 311 of LNCIS. Springer-Verlag, Ch. 2, pp. 23–64.

Mahony, R., Hamel, T., Pflimlin, J. M., 2008. Nonlinear complementary filters on the special orthogonal group. IEEE Transactions on Automatic Control 53 (5), 1203–2018.

Mohleji, S. C., Wang, G., September 2010. Modeling ADS-B position and velocity errors for airborne merging and spacing in interval management application. https://www.mitre.org/publications/technical-papers/, The MITRE Corporation, 7515 Colshire Drive, McLean VA 22102.

Perez, T., 2005. Ship Motion Control: Course Keeping and Roll Stabilisation Using Rudder and Fins. Advances in Industrial Control. Springer-Verlag London Ltd.

Richter, M., Schneider, K., Walser, D., Sawodny, O., 2014. Real-time heave motion estimation using adaptive filtering techniques. In: Proc. of the 19th IFAC World Congress. Cape Town, South Africa, pp. 10119–10125.

Sælid, S., Jenssen, N. A., Balchen, J. G., 1983. Design and analysis of a dynamic positioning system based on the Kalman filtering and optimal control. IEEE Transactions on Automatic Control 28 (3), 331–339.

SNAME, 1950. Nomenclature for treating the motion of a submerged body through a fluid. In: Technical and Research Bulletin No. 1—5. The Society of Naval Architects and Marine Engineers, New York, pp. 1–15.

Titterton, D. H., Weston, J. L., 2004. Strapdown inertial navigation technology, 2nd Edition. Institution of Electrical Engineers and American Institute of Aeronautics and Astronautics.

van Loan, C. F., 1978. Computing integrals involving the matrix exponential. IEEE Trans. Automatic Control AC–23 (3), 395–404.

Welch, P. D., 1967. The use of fast fourier transform for the estimation of power spectra: A method based on time averaging over short, modified periodograms. IEEE Transactions on Audio and Electroacoustics 15 (2), 70–73.